



# Modelling the transport and deposition of ash following a magnitude 7 eruption: the distal Mazama tephra

Hannah M. Buckland<sup>1,2</sup> · Larry G. Mastin<sup>3</sup> · Samantha L. Engwell<sup>4</sup> · Katharine V. Cashman<sup>1,5</sup>

Received: 14 February 2022 / Accepted: 20 July 2022 / Published online: 2 September 2022  
© The Author(s) 2022

## Abstract

Volcanic ash transport and dispersion models (VATDMs) are necessary for forecasting tephra dispersal during volcanic eruptions and are a useful tool for estimating the eruption source parameters (ESPs) of prehistoric eruptions. Here we use Ash3D, an Eulerian VATDM, to simulate the tephra deposition from the ~7.7 ka climactic eruption of Mount Mazama. We investigate how best to apply a VATDM using the ESPs characteristic of a large magnitude eruption ( $M \geq 7$ ). We simplify the approach to focus on the distal deposit as if it were formed by a single phase of Plinian activity. Our results demonstrate that it is possible to use modern wind profiles to simulate the tephra dispersal from a prehistoric eruption; however, this introduces an inherent uncertainty to the subsequent simulations where we explore different ESPs. We show, using the well-documented distal Mazama tephra, that lateral umbrella cloud spreading, rather than advection–diffusion alone, must be included in the VATDM to reproduce the width of the isopachs. In addition, the Ash3D particle size distribution must be modified to simulate the transport and deposition of distal fine-grained ( $< 125 \mu\text{m}$ ) Mazama ash. With these modifications, the Ash3D simulations reproduce the thickness and grain size of the Mazama tephra deposit. Based on our simulations, however, we conclude that the exact relationship between mass eruption rate and the scale of umbrella cloud spreading remains unresolved. Furthermore, for ground-based grain size distributions to be input directly into Ash3D, further research is required into the atmospheric and particle processes that control the settling behaviour of fine volcanic ash.

**Keywords** Volcanic ash cloud · Atmospheric dispersion · Eruption source parameters · Umbrella cloud spreading · Tephra

## Introduction

Predicting the transport and deposition of volcanic ash following a large magnitude explosive volcanic eruption poses an unprecedented challenge for hazard mitigation (Newhall et al. 2018). Whilst volcanic ash transport and dispersion models (VATDMs) have undergone increased testing and

validation since the 2010 eruption of Eyjafjallajökull in Iceland (e.g. Bonadonna et al. 2012; Gudmundsson et al. 2012; Hort 2016; Beckett et al. 2020), these advances have been informed by observations associated with recent, relatively small magnitude eruptions (e.g. Dacre et al. 2011; Folch et al. 2012; Osorio et al. 2013; Magill et al. 2015; Mastin et al. 2016; White et al. 2017). Large eruptions, in contrast, can have multiple phases of activity (e.g. Sigurdsson and Carey 1989; Rosi et al. 1999; Perrotta and Scarpato 2003; Marti et al. 2016; Madden-Nadeau et al. 2021), a large fine-ash fraction (Rose and Durant 2009; Engwell and Eychenne 2016), extreme erupted volumes (Froggatt 1982; Matthews et al. 2012; Johnston et al. 2014; Buckland et al. 2020) and complex plume dynamics (Baines and Sparks 2005; Costa et al. 2014, 2018; Pouget et al. 2016; Barker et al. 2019), all of which pose a challenge for existing VATDMs. No magnitude ( $M$ ; on the scale of Pyle 2000) 7 or greater eruptions have occurred since volcanoes have been observed using satellite remote sensing ( $> 1970\text{s}$ ). Therefore, unlike recent smaller eruptions where the eruption source parameters

Editorial responsibility: M.I. Bursik

✉ Hannah M. Buckland  
hannah.buckland@bristol.ac.uk

- <sup>1</sup> School of Earth Sciences, University of Bristol, Wills Memorial Building, Bristol, UK
- <sup>2</sup> Department of Geography, Swansea University, Singleton Campus, Swansea, UK
- <sup>3</sup> U.S. Geological Survey, Vancouver, WA, USA
- <sup>4</sup> British Geological Survey, The Lyell Centre, Edinburgh, UK
- <sup>5</sup> Department of Earth Sciences, University of Oregon, Eugene, OR, USA

(ESPs), such as plume height and mass eruption rate (MER), can be determined using remote sensing techniques (Holasek et al. 1996; Bonadonna et al. 2011; Osorio et al. 2013), the ESPs for large prehistoric eruptions are based on the interpretation of field deposits, which can introduce significant uncertainty (Biass and Bonadonna 2011; Engwell et al. 2013; Klawonn et al. 2014; Bonadonna et al. 2015; Buckland et al. 2020).

Hazards associated with the dispersion and deposition of volcanic ash following a large magnitude eruption will be unlike anything experienced in modern times because of the high concentration of ash in the atmosphere ( $> 4 \text{ mg/m}^3$ , the no-fly zone limit set by the European Commission; Stohl et al. 2011; Gouhier et al. 2019) and the very large areas impacted by ash fall ( $\sim$  millions of  $\text{km}^2$ ). Ash in the atmosphere disrupts aviation, impacts local meteorology and can interfere with telecommunication signals (e.g. Casadevall 1994; Durant et al. 2009; Prata and Tupper 2009; Wilson et al. 2012; Lechner et al. 2017). Once ash is deposited, it can cause roof collapse and damage to agriculture and infrastructure, including electrical transmission networks and roads (e.g. Wilson et al. 2012; Waitt 2015; Blake et al. 2016; Blong et al. 2017). Volcanic ash also poses a health hazard and can contaminate water supplies (e.g. Horwell and Baxter 2006; Stewart et al. 2006; Horwell 2007). Complete ash removal following a large eruption is impossible so ash hazards will be long-lived, particularly as ash is continually remobilised by wind, water and hillslope processes (e.g. Hadley et al. 2004; Wilson et al. 2011; Liu et al. 2014; Pierson and Major 2014; Panebianco et al. 2017). The longevity of ash hazards will amplify the societal impacts of a large eruption. For example, increased demand for limited resources, food shortages following contamination and/or disruption of supply chains can lead to civil unrest and even societal collapse (Nel and Righarts 2008; Wilson et al. 2012; Newhall et al. 2018). Indeed, archaeological evidence suggests that the Mazama eruption, combined with climate change, caused the inhabitants of the northern Great Plains to abandon their homelands for 500–600 years following the eruption (Oetelaar and Beaudoin 2016). Therefore, it is paramount for hazard prediction and risk mitigation efforts to develop VATDMs that can produce meaningful forecasts of ash dispersal from magnitude 7 and greater scenarios. These simulations can then be combined with magnitude frequency distributions for volcanic eruptions to produce probabilistic hazard assessments at volcanoes that have the potential to produce large eruptions (Connor et al. 2001; Jenkins et al. 2012; Sheldrake 2014; Rougier et al. 2018).

Here, we simulate the climactic Mazama eruption with the Eulerian ash dispersion model Ash3D (Schwaiger et al. 2012). VATDMs simplify the complex physical processes that disperse and deposit volcanic ash and therefore cannot perfectly reconstruct the ash dispersion of the  $\sim 7.7$ -ka

climactic Mazama eruption. However, the primary goal is to highlight areas where Ash3D can successfully replicate features of the deposit and where the model simulations cannot explain the observed tephra distribution. The well-documented Mazama tephra deposit offers an excellent opportunity for this endeavour because of the extensive field data available for model validation. Our results help to identify the features unique to large explosive eruptions that are not well captured by VATDM modelling approaches that have largely been tested using smaller eruptions. We then discuss reasons why Ash3D simulations differ from the field data from the perspectives of both implicit simplifications of VATDMs and uncertainties in the field data.

## Background

### The Mazama climactic eruption and tephra deposit

Mount Mazama was a stratovolcano in the volcanic arc of the Cascade Range that underwent a climactic caldera-forming eruption  $\sim 7.7$  ka to create modern-day Crater Lake, Oregon, USA. Eruption of more than  $60\text{-km}^3$  dense-rock equivalent (DRE) of rhyodacite magma deposited tephra across  $> 1$  million  $\text{km}^2$  of north-western North America (Williams 1942; Lidstrom 1971; Bacon 1983; Bacon and Druitt 1988; Druitt and Bacon 1989; Young 1990; Jensen et al. 2019; Buckland et al. 2020). Studies of the proximal ( $< 100$  km from source) eruption sequence have substantially advanced our understanding of caldera collapse and the evolution of complex magmatic systems (e.g. Williams 1942; Williams and Goles 1968; Bacon 1983; Bacon and Druitt 1988; Druitt and Bacon 1989; Young 1990; Klug et al. 2002; Wright et al. 2012; Karlstrom et al. 2015). The dominant tephra dispersal direction towards the east and northeast of the vent (Fig. 1) means that the widespread distal Mazama tephra forms an important Holocene isochron across much of the northwestern conterminous USA and Canada, which has aided correlation and dating of countless sedimentary sequences, archaeological finds and paleoseismic events (e.g. Cressman et al. 1960; Abella 1988; Long et al. 1998; Oetelaar and Beaudoin 2016; Jensen et al. 2019; Buckland et al. 2020). The tephra is also an important cryptotephra (non-visible) isochron in northeastern Canada, the USA and the GISP2 ice core (Hammer et al. 1980; Zdanowicz et al. 1999; Pyne-O'Donnell et al. 2012; Spano et al. 2017; Jensen et al. 2021). The widespread subaerial tephra deposit also provides an excellent opportunity to validate the outputs of VATDMs against field observations.

The climactic Mazama eruption had two main eruptive phases. A thick and well-sorted fall deposit records an initial Plinian phase (Williams and Goles 1968; Bacon 1983; Young 1990) which was followed by an ignimbrite

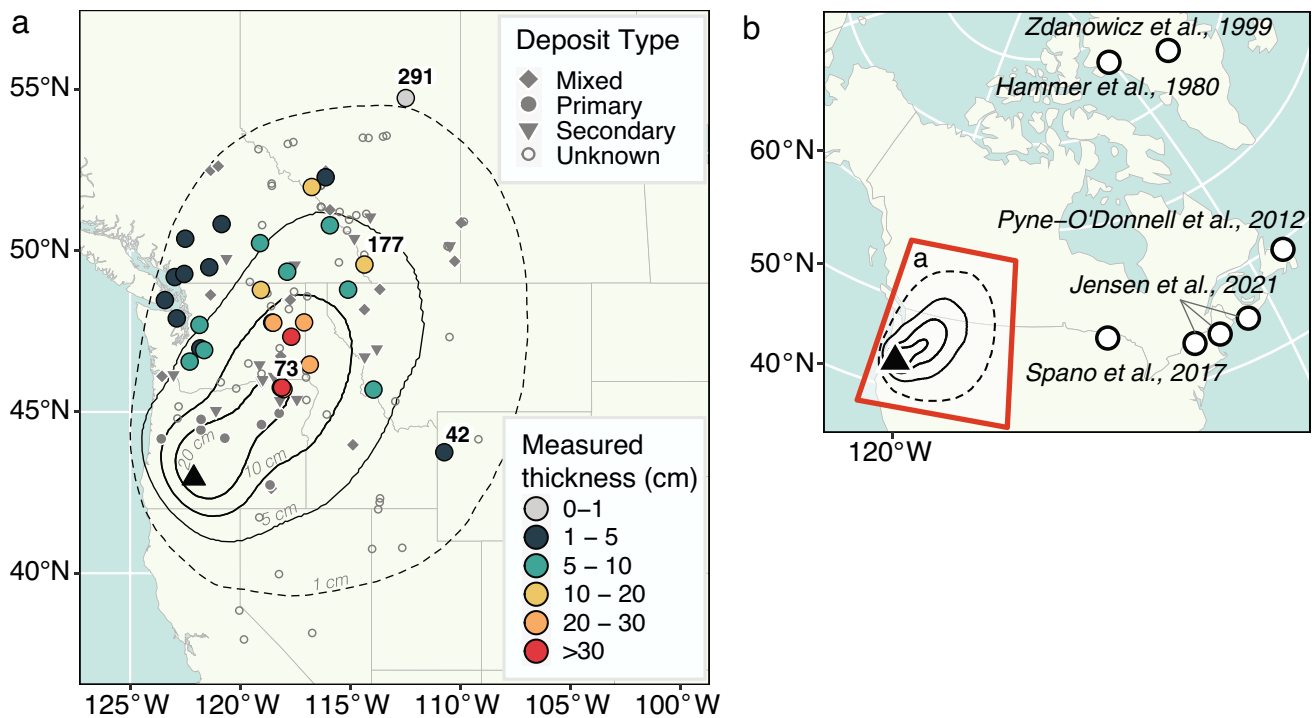


**Fig. 1** Locations where the Mazama tephra has been recorded. **a** Isopachs of the distal deposit, and sites in the USA and Canada where Mazama tephra has been recorded >130 km from source (Buckland et al. 2020; see Supplementary Table S4). The symbol represents the deposit type with the larger coloured points corresponding to sites where the tephra thickness is measured and has experienced minimal

remobilisation since deposition (Buckland et al. 2020). The numbered sites are key sites referenced in this study. **b** A map showing the location of map **a** and seven ultra-distal sites (>1500 km from source) containing Mazama cryptotephra. Each site is labelled with the relevant reference

forming phase and accompanying caldera collapse (Bacon 1983; Druitt and Bacon 1986). The latter phase produced a proximal lithic lag breccia (Druitt and Bacon 1986) and large (~29 km<sup>3</sup> DRE) pyroclastic density currents (PDC) that reached >70 km from source. Both phases erupted magma of similar composition except for the final PDCs of the caldera collapse phase, which were more mafic (Bacon 1983). For this reason, it is not possible to determine the relative proportion of original Plinian and later co-PDC contributions to the distal fine ash, which records the same rhyodacitic composition (Young 1990; Buckland 2022). For simplicity, we therefore treat the entire distal deposit as part of one Plinian eruptive phase and use continuous meteorological data for the simulation.

### Modelling large volcanic eruptions

Modelling the dispersal of volcanic ash from an eruption of large magnitude ( $M \geq 7$ ) is considerably more complex than for smaller magnitude ( $M \leq 5$ ) events for multiple reasons. Firstly, the high MERs that occur during large eruptions mean that gravity currents are commonly formed as the plume reaches neutral buoyancy in the atmosphere, and the

plume spreads by buoyancy forces close to source rather than solely by advection–diffusion (Bursik et al. 1992; Woods and Kienle 1994; Sparks et al. 1997; Costa et al. 2013). Gravitational spreading in the umbrella cloud region affects tephra dispersion but is typically not accounted for in VATDMs or applied in the reproduction of past events (Woods and Wohletz 1991; Sparks et al. 1997; Suzuki and Koyaguchi 2009; Costa et al. 2013; Pouget et al. 2016). Moreover, the distance from source over which gravitational spreading dominates tephra transport during large eruptions is poorly constrained and may be much greater than what has been witnessed during (smaller) historical eruptions (Houghton et al. 2004; Costa et al. 2018; Constantinescu et al. 2021).

Secondly, large explosive eruptions, especially those with significant co-PDC phases, are associated with large volumes of fine ash. Analysis of trends of median grain size with distance (Engwell and Eychenne 2016; Cashman and Rust 2020; Buckland et al. 2021) show that the grain size of deposits initially decays with distance from source but then stabilises over large distances, a trend particularly well defined for large eruptions. The median grain size of these distal deposits is typically 30–60 μm (Engwell and Eychenne 2016), which results in a low particle settling velocity that

rarely exceeds the vertical component of air velocity (atmospheric turbulence). As a result, sedimentation of individual ash particles is suppressed and sedimentation requires other mechanisms, such as aggregation (Brown et al. 2012; Van Eaton et al. 2012; Rossi et al. 2021) or the formation of convective instabilities (Manzella et al. 2015; Scollo et al. 2017; Freret-Lorgeril et al. 2020). Because it is not trivial to consider such processes in VATDMs, significant assumptions must be made to invoke the settling behaviour of these fine particles in numerical models.

Thirdly, as exemplified by the Mazama eruption, large eruptions typically have multiple phases (e.g. Santorini ~ 3.6 ka, Sparks et al. 1983; Tabora 1815, Sigurdsson and Carey 1989; the Campanian Ignimbrite ~ 39 ka, Perrotta and Scarpati 2003; Engwell et al. 2014; Ilopango ~ 1.5 ka, Pedrazzi et al. 2019). This means that ESPs are highly variable and likely time dependent, which is extremely challenging to reconstruct from field deposits: for example, shifting wind conditions, varying MERs and unsteady plume heights. Furthermore, during caldera-forming eruptions, the vent geometry and location change significantly throughout the eruption, again causing the ESPs to vary with time (Legros et al. 2000; Smith et al. 2016; Suzuki et al. 2020). ESPs for co-PDC plumes are also poorly constrained. For example, co-PDC plumes cannot be approximated as a point source and the relationship between MER and the mass entering the plume may be significantly different from the Plinian phase (Woods and Wohletz 1991; Baines and Sparks 2005; Engwell et al. 2016; Costa et al. 2018; Pedrazzi et al. 2019).

Fourth, ESPs are necessarily derived from field deposits for prehistoric eruptions and thus have significant uncertainties because of data sparsity, post-eruptive remobilisation of deposits and deposit model approximations (Biass and Bonadonna 2011; Bonadonna et al. 2015; Buckland et al. 2020). These issues are particularly pertinent for large eruptions that deposit tephra across variable environments (e.g. submarine versus subaerial). Additionally, although in proximal regions it may be possible to identify deposits from individual phases of an eruption (e.g. Plinian versus co-PDC), in distal reaches (typically distances greater than several hundreds of kilometres for large explosive eruptions), deposits merge and it becomes impossible to separate these contributions (Engwell et al. 2014; Buckland 2022). This means that total grain size distributions (TGSDs and other field measurements such as deposit thickness) are integrated over multiple eruption phases.

Finally, simulation of volcanic plumes requires meteorological information. However, given the age of most large explosive eruptions, accurate meteorological data for the time of the eruptions are not available. Moreover, meteorological conditions can vary seasonally, and for most prehistoric eruptions, information on eruption seasonality is limited. We therefore use modern meteorological information

under the assumption that conditions have not changed significantly in the intervening time (Johnston et al. 2012).

### Ash3D model description and umbrella spreading regimes

Ash3D is a Eulerian, finite volume dispersion model that computes tephra transport and deposition across a 3D grid using a time-dependent wind field (Schwaiger et al. 2012; Mastin et al. 2013). The model does not include the dynamics of a rising plume. The standard model setup, which works well for weak plumes and sub-Plinian eruptions, approximates a volcanic plume by adding tephra above the vent as either a point source, vertical line source or (most commonly) some vertical distribution such as that of Suzuki (Suzuki 1983; Carey 1996; Fig. 2):

$$\frac{d\dot{M}}{dz} = \dot{M} \frac{k_s^2(1 - z/H_T)\exp(k_s(z/H_T - 1))}{H_T[1 - (1 + k_s)\exp(-k_s)]} \quad (1)$$

Here ( $\dot{M}$ ) is the mass flow rate into the column of cells that approximates the plume (Fig. 2a, b),  $H_T$  is the height of the plume top,  $z$  is the elevation at a particular point in the column and  $k_s$  is a constant that controls the mass distribution across cells (Fig. 2c).

For modelling large eruptions, several dispersal models now consider the dynamics of a growing umbrella cloud in spreading ash (Costa et al. 2013, 2017; Webster et al. 2020; Cao et al. 2021; Constantinescu et al. 2021). Ash3D calculates radial spreading at the neutral buoyancy elevation ( $H_u$ ; Fig. 2b; Mastin et al. 2014), following the formula of Costa et al. (2013, 2017), which assumes that the volume growth rate of the umbrella cloud ( $q$ ) is proportional to the mass eruption rate ( $\dot{M}$ ):

$$q = C\sqrt{k_e} \frac{\dot{M}^{\frac{3}{4}}}{N^{\frac{5}{4}}} \quad (2)$$

where  $k_e$  is the radial entrainment coefficient,  $C$  is a constant of proportionality and  $N$  is the Brunt-Väisälä, or buoyancy, frequency. In other words, the expansion of the umbrella cloud depends on the intensity of the volcanic input ( $\dot{M}$ ) and the atmospheric properties ( $k_e$ ,  $N$  and  $C$ ).  $C$  has been determined empirically to be  $\sim 0.43 \times 10^3 \text{ m}^3 \text{ kg}^{-3/4} \text{ s}^{-3/2}$  for tropical eruptions and  $0.87 \times 10^3 \text{ m}^3 \text{ kg}^{-3/4} \text{ s}^{-3/2}$  for polar and midlatitude eruptions (Suzuki and Koyaguchi 2009; Costa et al. 2013, 2017). We use  $C = 0.87 \times 10^3 \text{ m}^3 \text{ kg}^{-3/4} \text{ s}^{-3/2}$ ,  $k_e = 0.1$  and  $N = 0.02 \text{ s}^{-1}$  for the simulations (Table 1; Mastin et al. 2014).

The velocity field within the spreading umbrella cloud is calculated using the volume growth rate ( $q$ ) and the radial distance within the umbrella cloud ( $R$ ; for details see Appendix 1). The appropriate formula for calculating

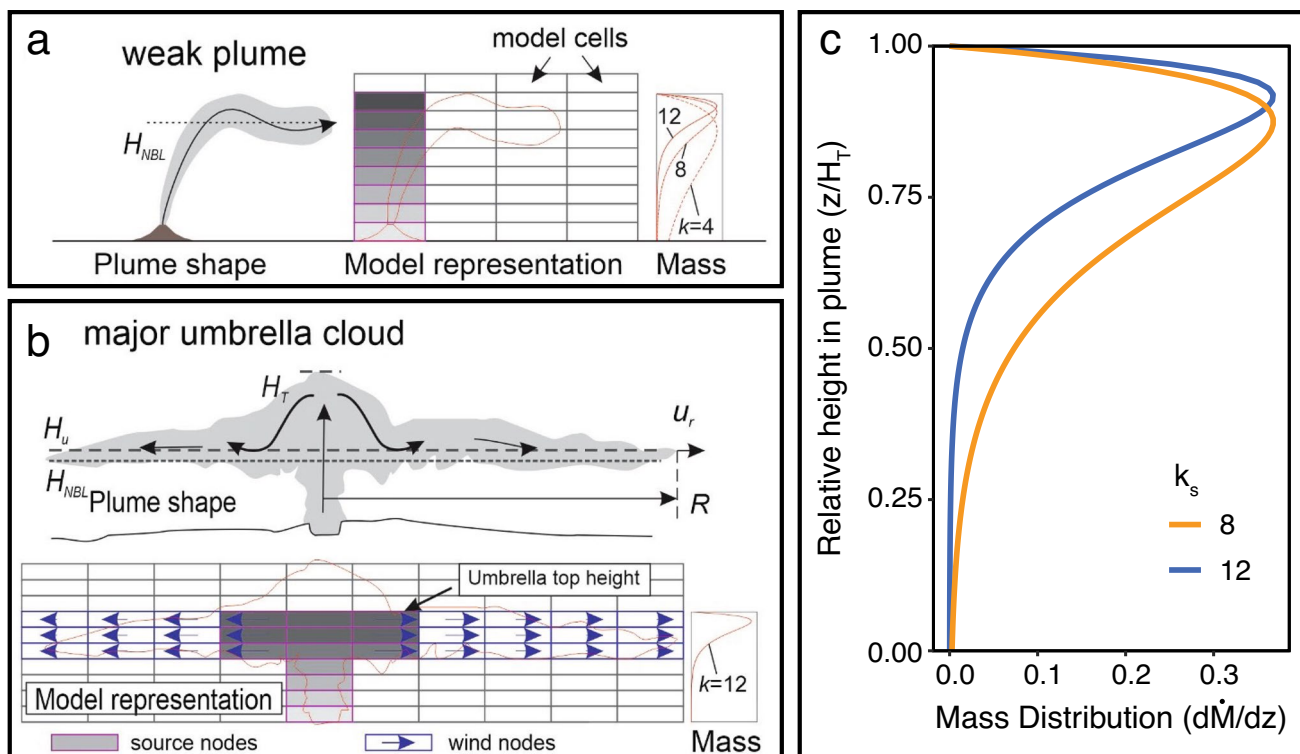


**Fig. 2** Model setups for different plume regimes using the Suzuki mass distribution in Ash3D. **a** Weak plume; **b** major umbrella cloud. Grey cells are source nodes that show where ash (mass) is added at each model time step. Plume **a** is approximated by a vertical column of model cells. Plume **b** includes a radial wind field shown by

nodes with blue arrows. The boxes on the right-hand side represent the Suzuki mass distribution in the plume shown in detail in panel **c**. **c** Suzuki probability density function used to distribute mass in the plume with different values of the constant  $k_s$  (Eq. 1). Panels **a–b** from Mastin and Van Eaton (2020)

radial velocity of the plume in the umbrella region is still the matter of some debate; in this study, we consider two options. First is the method of Costa et al. (2013; see their Eq. 11), implemented by Mastin et al. (2014) in Ash3D (Eq. 7 in Mastin et al. 2014) where the radial velocity within the umbrella cloud  $u_r$  is governed by:

$$u_r = u_R \left( \frac{3R}{4r} + \frac{r}{4R} \right), \tag{3}$$

where  $u_R$  is the velocity at the flow front and  $r$  is the position in the umbrella cloud (Appendix 1). Second is the formulation of Webster et al. (2020; see their Eq. 7):

$$u_r = u_R \left( \frac{R}{r} \right)^{\frac{1}{2}}. \tag{4}$$

The difference between the two spreading regimes is shown in Fig. 3. Both regimes meet the boundary condition that, when  $r \rightarrow R$ ,  $u_r \rightarrow u_R$  but Eq. 3 (Costa et al. 2013) gives higher radial spreading velocities when  $r \ll R$  (Fig. 2).

Once the mass is added to the cells, Ash3D computes mass concentration  $Q$  with time  $t$  using the formula:

$$\frac{\partial Q}{\partial t} + \nabla \cdot [(\vec{u}_a + \vec{v}_s)Q] - \nabla \cdot (K\nabla Q) = S. \tag{5}$$

where  $u_a$  is the 3D wind vector,  $v_s$  is the particle settling velocity,  $K$  is the diffusivity and  $S$  is the source term, which is non-zero only in the nodes above the volcano. The second and third terms on the left-hand side of this equation represent (1) advection by wind and settling, and (2) turbulent diffusion, respectively.

Using the umbrella spreading scheme at the beginning of the simulation, the mass flow rate into the umbrella cloud ( $q$ ) is calculated using Eq. 2. Ash is placed into the source nodes (grey nodes, Fig. 2b) and distributed vertically using a Suzuki distribution (Eq. 1) with  $k=12$ , which represents a top-heavy distribution of mass in the plume (Fig. 2c). Then, at each time step during the duration of the eruption, radial winds are calculated using Eqs. 3 or 4, added to the ambient wind field  $u_a$ , and the movement of ash across cell walls is calculated using Eq. 5. After the eruption ends, ash advection and diffusion continue to be calculated using Eq. 5, but no ash is added to the source nodes and radial winds are no longer added to the ambient winds.

**Table 1** Model parameters used for all simulations after resolving the best-fit wind profile. The parameters first used to resolve the wind profile are highlighted with an asterisk (\*)

Parameter	Value(s)
Eruption start time	2010 11 06 11:36 UTC
Duration	24 h
Erupted volume DRE	40 km <sup>3</sup>
Height of the top of umbrella cloud ( $H_u$ )	15, 25, 30* and 40 km
Inferred vent location	122.12°W <i>longitude</i> 42.93°N <i>latitude</i>
Model domain	90–135°W <i>longitude</i> 32.5–57.5°N <i>latitude</i>
Model resolution	0.5° <i>horizontally</i> 2 km <i>vertically</i>
GSD	GSD_M16*, GSD_M14, GSD_B21_B, GSD_B21_U (see Fig. 5)
Diffusion constant ( $K$ )	0*, 1000, 3000 and 10 000 m <sup>2</sup> s <sup>-1</sup>
Umbrella spreading regime	None, Webster et al. (2020) and Costa et al. (2013)* (see Fig. 3)
Deposit density ( $\rho_d$ )	700 and 1000* kgm <sup>-3</sup>
$k_e$	0.1
$N$	0.02 s <sup>-1</sup>
$C$	$0.87 \times 10^3 \text{ m}^3 \text{ kg}^{-3/4} \text{ s}^{-3/2}$
$\lambda$	0.2

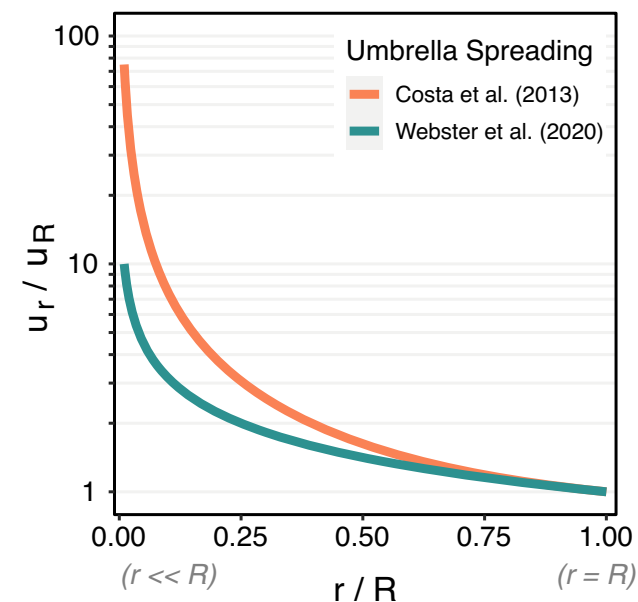


**Fig. 3** Different umbrella cloud radial wind formulations used in Ash3D. Ratio of position in umbrella cloud  $r$  to the radius of the umbrella cloud  $R$  plotted against the ratio of the radial wind velocity at position  $r$  ( $u_r$ ) to the velocity at the cloud front ( $u_R$ ). Formulations used are from Costa et al. (2013) and Webster et al. (2020)

## Ash3D model inputs

### Volcanic inputs—erupted volume, particle characteristics, eruption duration and plume height

The aim of this study is to model the dispersion of distal tephra; therefore, we exclude the volume contained in deposits < 130 km from source. In this way, we also avoid poor constraints on the volume of the proximal deposits because of overlapping eruptive units and the unknown volume contained within the caldera collapse deposits (Bacon 1983; Young 1990; Bacon and Lanphere 2006; Buckland et al. 2020). At the same time, by excluding the proximal deposit, we reduce uncertainty in Ash3D simulations caused by complex proximal deposition processes related to plume and edifice instabilities.

To estimate the bulk volume of the distal Mazama deposit, we use isopachs constructed using distal ash thicknesses and fit by a single exponential function to the square root of the isopach area against log of tephra thickness (Table S5; Pyle 1989; Fierstein and Nathenson 1992; Daggitt et al. 2014; Buckland et al. 2020). The bulk volume estimates range from 129 to 134 km<sup>3</sup> depending on whether distal isopachs are extrapolated back to the source (Fig. 4a) or include only the volume beyond the proximal isopachs (Fig. 4b). The DRE volume of the distal deposit is determined using the average deposit density (700 kgm<sup>-3</sup>) and magma density (2200 kgm<sup>-3</sup>) to give a minimum value of 40 km<sup>3</sup> DRE (Buckland et al. 2020; Buckland 2022).

The default GSD used by Ash3D is a simplified version of the TGSD of the May 1980 eruption of Mount St. Helens (Durant et al. 2009; Mastin et al. 2016). The TGSD is simplified by assigning all mass < 125  $\mu\text{m}$  to separate size classes in the Ash3D input file with lower density and more spherical shape factors than the coarser size fractions (Fig. 5a; Supplementary S3). In previous studies, this simplification is referred to as ‘aggregation’ (Mastin et al. 2014; 2016). Here we use the simplification to account for the range of processes that allow ‘premature’ (non-Stokes) fine ash sedimentation. Without this TGSD simplification, slow-settling particles (< 125  $\mu\text{m}$ ) do not deposit within the model domain (see Supplementary S2).

For comparison, we use the Ash3D default (GSD\_M16; Fig. 5a) in our simulations as well as three additional GSDs: (1) the GSD used by Mastin et al. (2014) when simulating a super-eruption from Yellowstone (GSD\_M14; Fig. 5b); (2) a bimodal TGSD based on the grain size of Mazama tephra deposits > 130 km from source (GSD\_B21\_B; Fig. 5c); and (3) a unimodal TGSD that reflects the grain size of the Mazama tephra > 400 km from source (GSD\_B21\_U; Fig. 5d; Buckland 2022). For GSD\_B21\_B

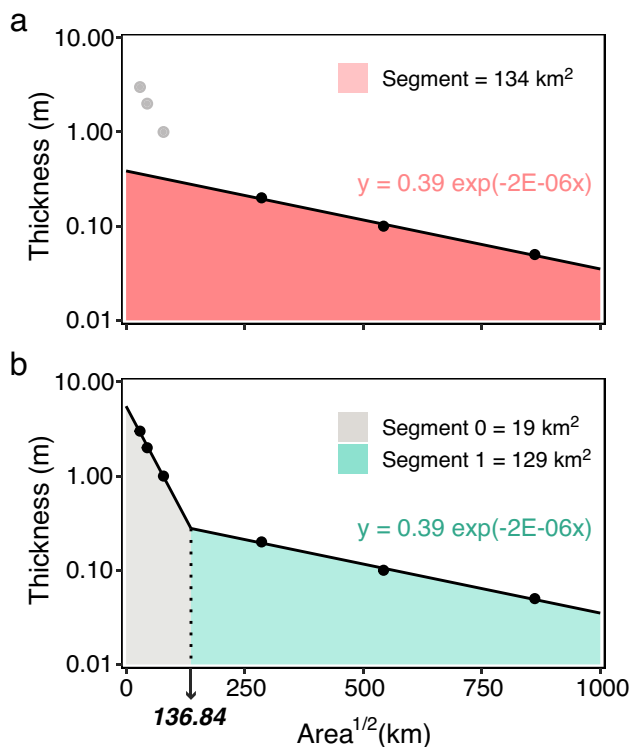


**Fig. 4** Exponential fits to square root area versus log thickness for Mazama isopachs. Isopachs drawn by Buckland et al. (2020). Bulk volume is calculated by finding the area under the exponential functions (Pyle 1989; Fierstein and Nathenson 1992). (a) One segment fit excluding the proximal isopachs. (b) Two exponential fits including data from Young (1990). The limit of integration for each segment is  $x = 136.84$

and GSD\_B21\_U, we treat the mass  $< 125 \mu\text{m}$  in the same way as the Ash3D default by assigning the mass into coarser size fractions which we refer to as simulated aggregates.

The particle densities for GSD\_M16 and GSD\_M14 have been taken from the literature (Mastin et al. 2014, 2016). For the simulations using GSD\_B21, we use the densities measured for Mazama samples in individual sieve fractions  $> 250 \mu\text{m}$  (Buckland et al. 2021). For particles  $\leq 250 \mu\text{m}$ , the particle density is equal to the glass density of the Mazama rhyodacite, which is  $\sim 2200 \text{kgm}^{-3}$  (Bacon 1983; Druitt and Bacon 1989). The simulated aggregate density is kept constant at  $600 \text{kgm}^{-3}$ , following Mastin et al. (2016).

We use a particle shape factor ( $F$ ) value of 0.65 for individual particles based on measurements made using Dynamic Image Analysis (DIA; Buckland et al. 2021). DIA measures the aspect ratio of particles ( $x_{c,\text{min}}/x_{F_e,\text{max}}$ ) which we equate to the 3D shape factor  $F$  used by Ash3D to calculate the particle drag coefficient according to the

formulation of Wilson and Huang (1979). The shape factor is determined by  $F = (b + c)/2a$ , where  $a$ ,  $b$  and  $c$  are the maximum, intermediate and minimum diameters of the particle. All simulated aggregates are assigned  $F = 1$  (Van Eaton et al. 2015; Mastin et al. 2016).

We use an eruption duration of 24 h in the Ash3D simulations. The actual duration of the climactic Mazama eruption is difficult to constrain without real-time observations using modern monitoring methods. Therefore, our estimate is based on the absence of evidence for an extended eruption duration. For example, there is no apparent erosion or soil development between the individual fall units or eruptive phases (Young 1990; Bacon and Lanphere 2006). The inferred duration of 24 h and erupted volume of  $40 \text{km}^3$  DRE gives a MER of  $1.46 \times 10^8 \text{kgs}^{-1}$ , which is within the range of  $\sim 10^8\text{--}10^{10} \text{kgs}^{-1}$  inferred and reconstructed for other large eruptions (e.g. Novarupta 1912, Fierstein and Hildreth 1992; Pinatubo 1991, Koyaguchi and Ohno 2001; Tambora 1815, Kandlbauer and Sparks 2014). It is lower than MER estimates from maximum lithic isopleths of the Mazama deposit ( $1 \times 10^8\text{--}3 \times 10^9 \text{kgs}^{-1}$ ; Young 1990); however, MER estimates from isopleths have not been validated for large magnitude eruptions because of a lack of observations. Furthermore, we note that our MER estimate is not representative of the actual MER because we only use the mass contained in the distal deposit rather than the total erupted mass.

In Ash3D simulations, the plume height used as model input is the top of the umbrella cloud rather than the top of the overshooting plume, under the assumption that the overshooting plume collapses gravitationally into the umbrella rather than being advected laterally with the ambient winds. The 15 June 1991 Pinatubo eruption, the closest historical analogue to a Mazama event, produced a plume with an overshooting top of 35–40 km and an umbrella top at about 25 km asl (Koyaguchi and Ohno 2001). Most of our simulations use an umbrella-top height of 30 km, but we also experimented with values of 15 and 40 km asl. The lower value of 15 km tests the impact of strong stratospheric winds above the tropopause on the dispersion (as seen at Mount St. Helens; Eychenne et al. 2015). Plume heights between 30 and 40 km were resolved by inversion modelling of the proximal Mazama deposits using Tephra2 (Suzuki 1983; Armienti et al. 1988; Bonadonna et al. 2005; Connor and Connor 2006; Biass 2018), as reported in Supplementary S1. Young (1990) estimated plume heights  $> 55 \text{km}$  from isopleths using the Carey and Sparks (1986) model. However, as with the MER estimates, these extreme heights reflect the limitations of the Carey and Sparks (1986) model that has not been validated with observations of the plumes from  $M > 7$  eruptions.

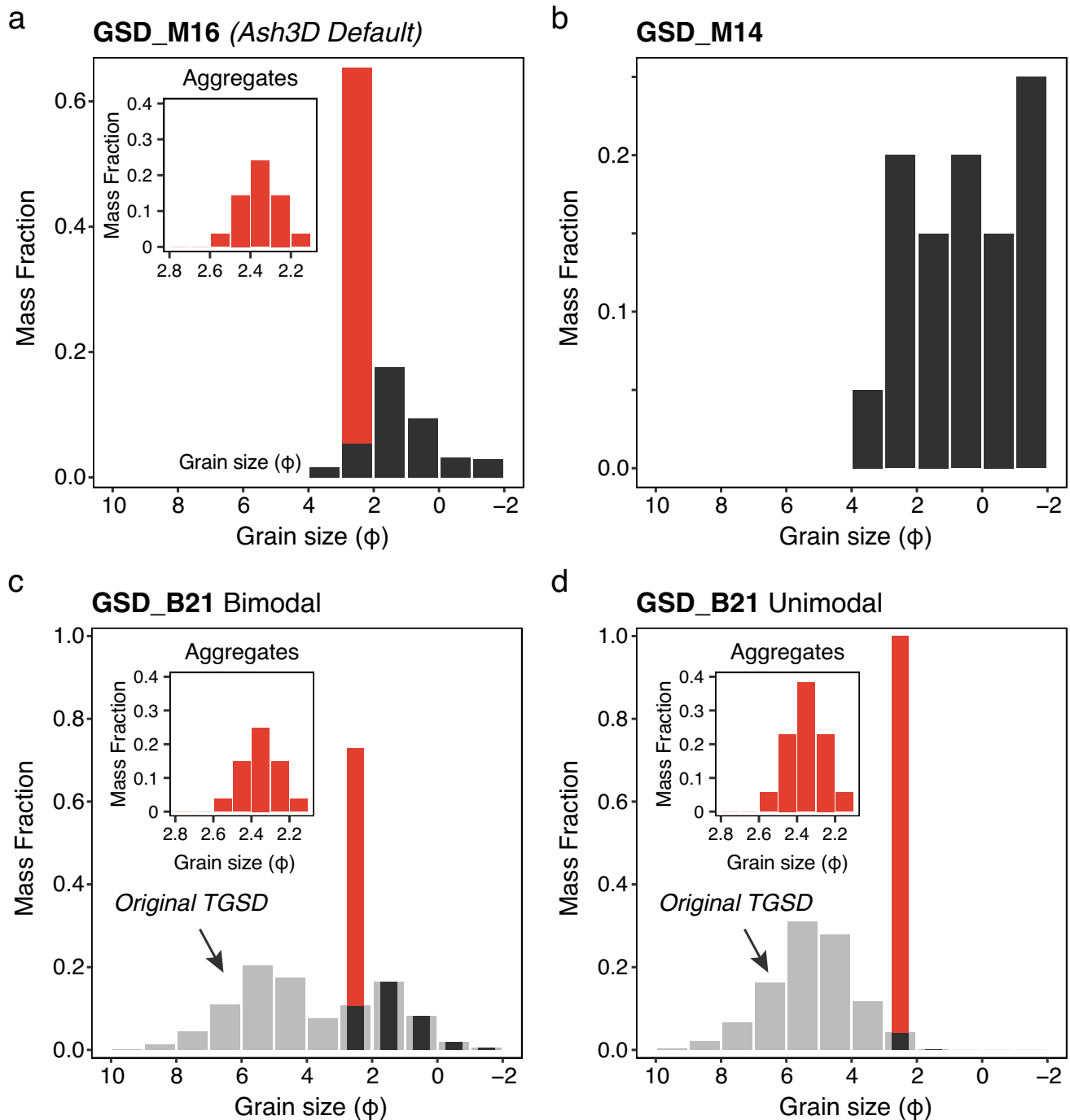


**Fig. 5** Grain size distributions (GSDs) used in Ash3D simulations. **(a)** The default GSD used by Ash3D referred to in the main text as GSD\_M16 (Mastin et al. 2016). The mass < 125  $\mu\text{m}$  is amalgamated into the simulated aggregate distribution shown in red. **(b)** The coarse GSD\_M14 from Mastin et al. (2014). **(c)** Bimodal TGSD of the

Mazama ash > 130 km from source (light grey) compared to the simplified GSD\_B21. **(d)** Unimodal TGSD of the Mazama ash > 400 km from source (light grey) and the simplified GSD\_B21. In panels c and d 100% of material < 125  $\mu\text{m}$  has been amalgamated into simulated aggregates size classes (red)

### Meteorological data and model parameters

The meteorological data used for the simulations are from the NOAA NCEP/NCAR Reanalysis 1 (RE1) model (Kalnay

et al. 1996), a global meteorological model extending from 1948 to the present with a horizontal resolution of 2.5 degrees latitude/longitude, temporal resolution of 6 h and 17 pressure levels from 1000 (sea level) to 10 millibars (~ 30 km

asl). Ash3D uses wind vectors, geopotential height and temperature from these models to calculate advection and particle fall velocities. For elevations above  $\sim 30$  km, Ash3D replicates the wind vectors at the highest RE1 model node. It then extrapolates temperature from the highest thermal lapse rate and pressure by integrating  $\rho g dz$ , where  $\rho$  is calculated from the ideal gas law. Average wind data for Mount Mazama (Crater Lake) over the period from 1990–2010 are shown in Fig. 6. Although winds below 5 km elevation are slow and variable in direction, at 6–14 km they are dominantly towards the east and are fastest ( $28 \pm 16 \text{ ms}^{-1}$ ) around the tropopause at 10–11 km (Fig. 6a). At higher elevation, velocities decrease and directions become bimodal towards both the east and west (Fig. 6b).

Using the fixed ESPs listed in Table 1, we ran the Ash3D simulation 800 times under different wind conditions and output the tephra thicknesses at each sampling site (Fig. 7). The simulation with a start time of 06 November 2010, 11:35 UTC, had the best visual agreement in the direction of the dispersal axis and thinning rate with distance (Fig. 7d). Interestingly, the wind profile relating to November supports evidence from pollen records that the Mazama eruption occurred during the northern hemisphere autumn (Mehring et al. 1977). More generally, this also shows that for eruptions from the mid-Holocene ( $\sim 8$  ka) in North America, modern reanalysis meteorological data can be appropriate for simulating ash dispersal. A comparison of this run with three others, randomly chosen from the 800, is shown in Fig. 7. We stress that Fig. 7 shows the simulated deposit using a fixed set of ESPs and should be viewed as separate to subsequent figures where we examine the sensitivity of the simulation to changing ESPs.

Turbulent diffusion is treated as a constant in Ash3D ( $K$  in Eq. 5) and is calculated using an implicit Crank-Nicolson method (Schwaiger et al. 2012). The amount of turbulent diffusion reflects complex and competing atmospheric processes, meaning that the value of  $K$  cannot be directly related to a single physical process (Schwaiger et al. 2012). When diffusivity is set to zero, Ash3D simulations run about three times faster and can produce realistic-looking results (Schwaiger et al. 2012). For this reason, diffusivity is set to zero in operational simulations (<https://vsc-ash.wr.usgs.gov>) when speed is important. In systematic comparisons, however, we see that diffusion-free simulations can produce deposits that are slightly narrower than mapped ones and may underestimate thickness in distal areas, even when adjusted for finer grain sizes (Mastin et al. 2016, 2020). Therefore, we run the Mazama simulations using different values of  $K$  ( $0$ – $10,000 \text{ m}^2\text{s}^{-1}$ ; Table 1) to account for the fact that  $K$  reflects multiple physical processes, including entrainment into the plume, and that for large eruptions, these processes are likely spatially varied and complex. The range of  $K$  explored is informed by the range of diffusion

coefficients for multiple advection–diffusion models from previous studies (e.g. Macedonio et al. 1988; Folch et al. 2008; Costa et al. 2008; Bonasia et al. 2011; Poulidis et al. 2018; Constantinescu et al. 2022).

## Results

We ran 57 simulations of the climactic Mazama eruption using the best-fit wind profile to explore the sensitivity of Ash3D to critical ESPs: the diffusivity constant ( $K$ ; Fig. 8), the deposit density ( $\rho_d$ ; Fig S5), the umbrella cloud spreading regime (Fig. 9), the height of the umbrella top ( $H_u$ ; Fig. S6) and the GSD (Fig. 10). The range of model parameters is reported in Table 1 and run specific inputs used in benchmark simulations are listed in Table 2. The results of changing the  $\rho_d$ ,  $H_u$  and GSD simplification are presented in Supplementary S2 for brevity. A full inventory of the simulations can be found in Supplementary Table S7. Here we describe the impact of changing the individual input parameters (the “Sensitivity to model inputs” section) and comment on the ability of the model to replicate the deposit thickness and GSD at specific localities (the “Comparing Ash3D outputs to the Mazama tephra deposit” section).

### Sensitivity to model inputs

To visualise the Ash3D outputs in this section, we plot a map of primary Mazama tephra localities (Buckland et al. 2020) with an opaque isopach map of the simulated deposit (Figs. 8, 9 and 10). The colour of each locality indicates the observed thickness; the same colour scheme is used for the shaded isopachs of the simulated deposit. In Figs. 8 and 9, we also plot the square root of the isopach area against the isopach thickness and fit an exponential function to the data (Pyle 1989). We refer to these as ‘Pyle plots’ in the figure captions for brevity.

Increasing the diffusivity constant  $K$  promotes turbulent diffusion and as a result the tephra is spread out over a larger area when  $K > 0 \text{ m}^2\text{s}^{-1}$  (Fig. 8). This supports assessments from simulations of other eruptions, where higher  $K$  increases spreading perpendicular to the main dispersal axis (Schwaiger et al. 2012; Mastin et al. 2016). Increasing  $K$ , however (Fig. 8b, c), does not produce the width of the deposit perpendicular to the main dispersal axis (off-axis) that we observe in isopachs constructed from Mazama field data (Fig. 1; Buckland et al. 2020). The pronounced area of secondary thickening seen in Fig. 8a reflects the bimodality of the default GSD (Fig. 5a). GSD\_M16 has a coarse mode at  $250 \mu\text{m}$  ( $2 \phi$ ) made up of individual particles and a second mode that corresponds to the simulated aggregates which are the size class concentrated in the zone of secondary thickening.

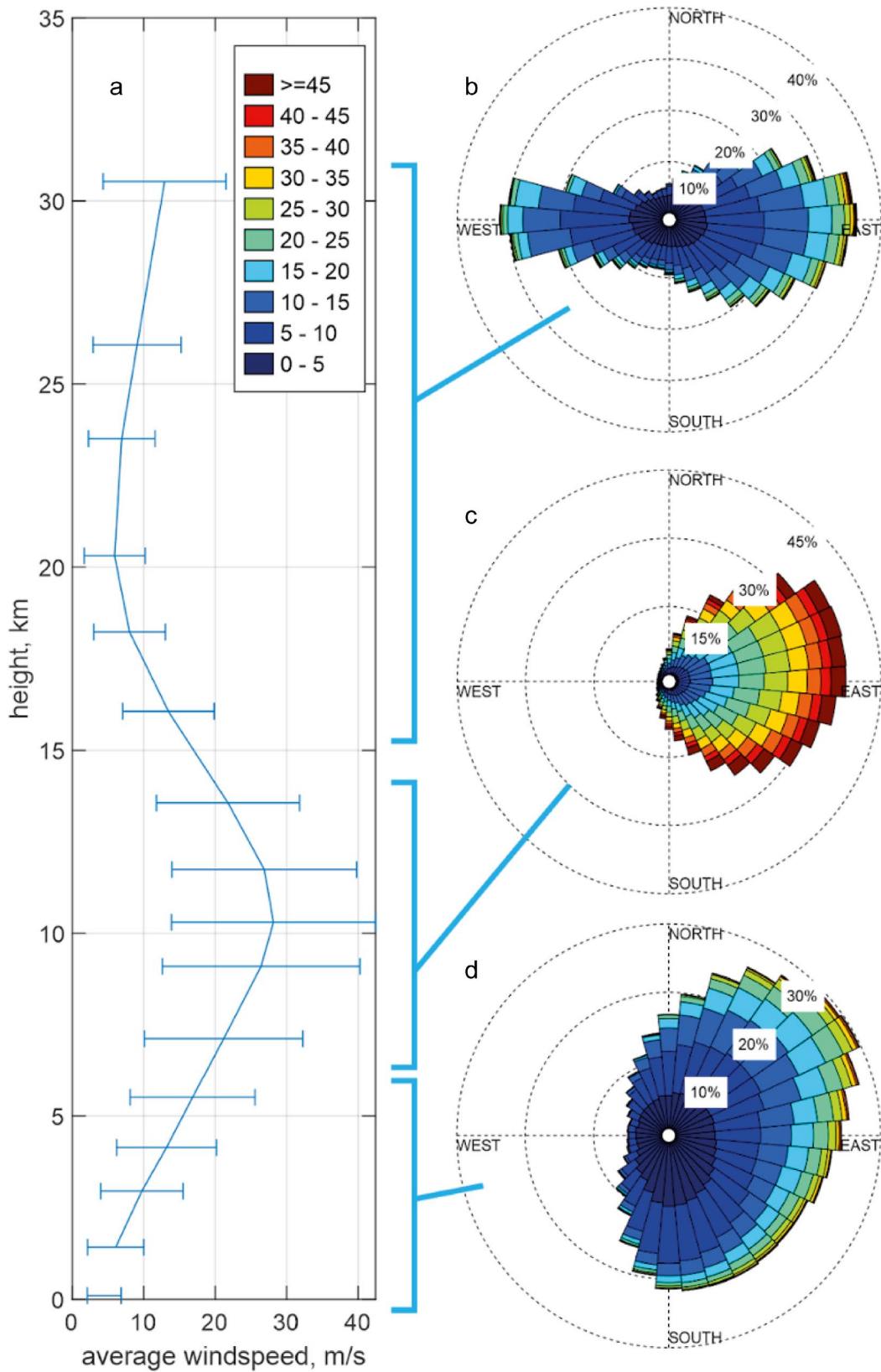


**Fig. 6** Summary wind data for 20 years at Crater Lake. **(a)** Wind speed ( $\text{ms}^{-1}$ ) versus elevation above sea level at Crater Lake based on NCEP Reanalysis 1 data for 1990–2010. Error bars are plus and minus one standard deviation. **(b–d)** Wind rose plots for the elevation ranges indicated, based on the same dataset. Pie segments depict the direction towards which the wind is blowing

Simulating umbrella spreading disperses tephra over a larger area compared to simulations where the ash is transported purely by advection diffusion coupled to the meteorological winds (Fig. 9). Simulations with no horizontal umbrella spreading produce an elongated deposit (Fig. 9a) with minimal off-axis spreading whereas wider isopachs are produced when umbrella winds are added to the ambient wind field. The amount of off-axis spreading depends on the formulation used to calculate the radial wind speeds (Eq. 4; Fig. 9b and Eq. 3; Fig. 9c). The area enclosed by the 10-mm isopach is greater when using the formula from Costa et al. (2013) at  $1.3 \times 10^6 \text{ km}^2$  compared to the Webster et al. (2020) formula where the same isopach encompasses  $1 \times 10^6 \text{ km}^2$ .

The GSD used significantly impacts the Ash3D simulations (Fig. 10). The Ash3D default GSD (GSD\_M16; Fig. 5a) produces isopachs that closely match those mapped from field deposits (Figs. 1a and 10a). Simulations using the coarsest GSD (GSD\_M14 from Mastin et al. 2014; Fig. 5b) produce the smallest area of tephra deposition due to rapid deposition of coarse particles close to source (Fig. 10b). Simulations using GSD\_B21\_B (Fig. 5c) produce similar 10-mm isopachs to runs using the default GSD, but the 200-mm isopach (orange) extends farther out to the northeast of the vent (Fig. 10c). However, sites where the observed thickness is  $> 200 \text{ mm}$  (red- and orange-filled circles) still lie outside of the simulated 200-mm isopach. GSD\_B21\_U (Fig. 5d) is a unimodal distribution that has been artificially ‘aggregated’ and is therefore effectively modelling the fallout of a single size class that does not deposit close to the vent. Interestingly, the thickness maximum for deposition of GSD\_B21\_U corresponds to sites where the observed distal thicknesses exceed 200 mm (Fig. 10d).

### Comparing Ash3D outputs to the Mazama tephra deposit

To visualise the differences between the thickness of the modelled deposit and field measurements of tephra thickness (Buckland et al. 2020), we plot the modelled and observed thickness at 30 localities on log–log plots. This ensures that differences in the thickness of distal, thinner deposits are evident (Fig. 11). We also include the equivalent plot using linear axes (Fig. 12), which helps visualise the differences in thicker, more proximal deposits as well as the differences between different simulations. For each simulation, we calculate the coefficient of determination ( $R^2$ ) and root mean square error (RMSE; see Supplementary Table S7). Comparing  $R^2$  and RMSE

values across the whole suite of simulations, however, is challenging because measures of goodness of fit can be biased by the proximal data where the absolute thickness values are greatest. For example, Run001 has the highest  $R^2$  value of all the simulations which indicates good agreement between the simulated and field deposit. However, we see from the high RMSE value and visual inspection of the simulated versus field-derived isopachs that this combination of ESPs in fact only matches the thickest field sites and the fit to the distal sites is relatively poor. Therefore, we use a qualitative assessment of the  $R^2$ , RMSE and visual comparison of simulated deposit to determine whether individual simulations fit the field data well.

The simulated thicknesses are within 4 and 0.25 times the observed thickness at 35 of the 36 primary localities for all the simulations that use the best-fit wind profile, excluding those that use GSD\_M14 (Figs. 11b and 12b). This suggests that the Ash3D simulations are reproducing the Mazama deposit reasonably well. For example, we know from lake core records that at least 0.1-cm ash was deposited at Lofty Lake, Alberta, Canada,  $> 1500 \text{ km}$  from source (site 291, Fig. 1a; Lichti-Federovich 1970; Lidstrom 1971; Young 1990; Buckland et al. 2020). All the Ash3D simulations disperse at least 1 mm of ash to Lofty Lake evidencing that the simulations can reproduce the long-range transport of ash that is inferred from field deposits.

Simulations that use the GSDs reconstructed from field data best replicate the thickness of deposits along the main dispersal axis when compared to runs where all other ESPs are the same except the GSD as indicated by the lower RMSE values (e.g. Figures 11 and 12). For example, at site 73, we measured 30 cm of primary Mazama tephra (Buckland et al. 2020). Using GSD\_B21\_U, Ash3D forecasts 26–37 cm of ash deposition at site 73 depending on the deposit density ( $\rho_d$ ) used (Run030; Figs. 11d and 12d). In contrast, all the simulations using GSD\_M14 and GSD\_M16 predict  $< 30 \text{ cm}$  at site 73 irrespective of assumed  $\rho_d$ . This suggests that the fine ash that is recorded at these sites has settling properties similar to the simulated aggregates.

Ash3D outputs the GSD at specified locations, which we compare to the GSD measured at that locality (Fig. 13). Excluding the simulations using GSD\_B21\_U, which contains no coarse material, all simulations predict coarser particles reaching further from source than observed in the field deposits. For example, using DIA and laser diffraction, we know that at site 73 particles  $> 250 \mu\text{m}$  account for  $< 1\%$  of the sample volume. However, simulations using the default GSD\_M16 (Run006; Fig. 13a), the coarse GSD\_M14 (Run014; Fig. 13b) and GSD\_B21\_B (Run022; Fig. 13c) predict that particles  $> 250 \mu\text{m}$  are being deposited at that distance from source. This is shown in Fig. 13 where the

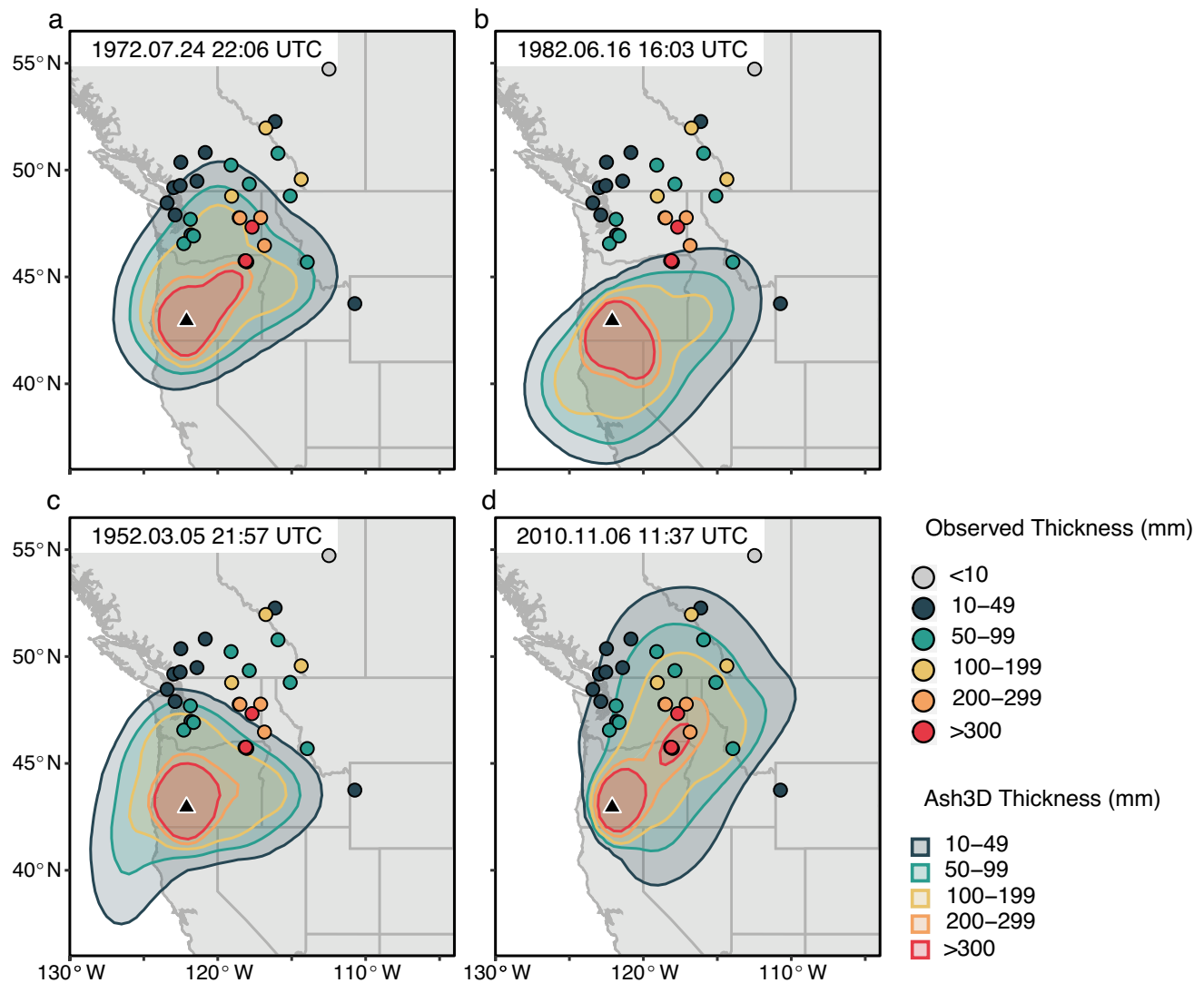


**Fig. 7** Illustration of the effect of different wind conditions on the deposit distribution. Simulations in (a–d) use the same source parameters but different eruption start times, indicated on each plot. The wind field in (d) was used for further sensitivity tests. The coloured

polygons in a–d represent the model isopachs and coloured dots represent measured sample thicknesses. All runs use source parameters in Table 1. Profiles of wind speed and direction with height for each simulation can be found in the supplementary material (Table S8)

black bars (simulated coarse particles) are higher than the GSD measured from field deposits (light grey).

## Discussion

Here we use the results of the Ash3D simulations of ~7.7 ka Mazama tephra deposit to consider the application of VATDMs to tephra deposits produced by large magnitude eruptions. We also discuss reasons that the application of VATDMs is unable to reproduce all the features of complex deposits such as the Mazama tephra, including both uncertainty in ESPs and inherent model simplifications.

## Considering the Mazama tephra case study

Before we could investigate the sensitivity of the Ash3D simulations, we first had to source appropriate meteorological reanalysis data that would reproduce the overall dispersal direction of the Mazama tephra towards the northeast of Crater Lake as we found that the wind data used strongly affected the overall dispersal (Fig. 7). We also simplified the Ash3D simulations by modelling only one explosive phase and thus using a relatively short period of wind data. Simplifying the meteorological data used is an inherent source of uncertainty throughout this study and could explain why the modelled deposit does not correspond perfectly to the field data in some locations. For example, lake core records

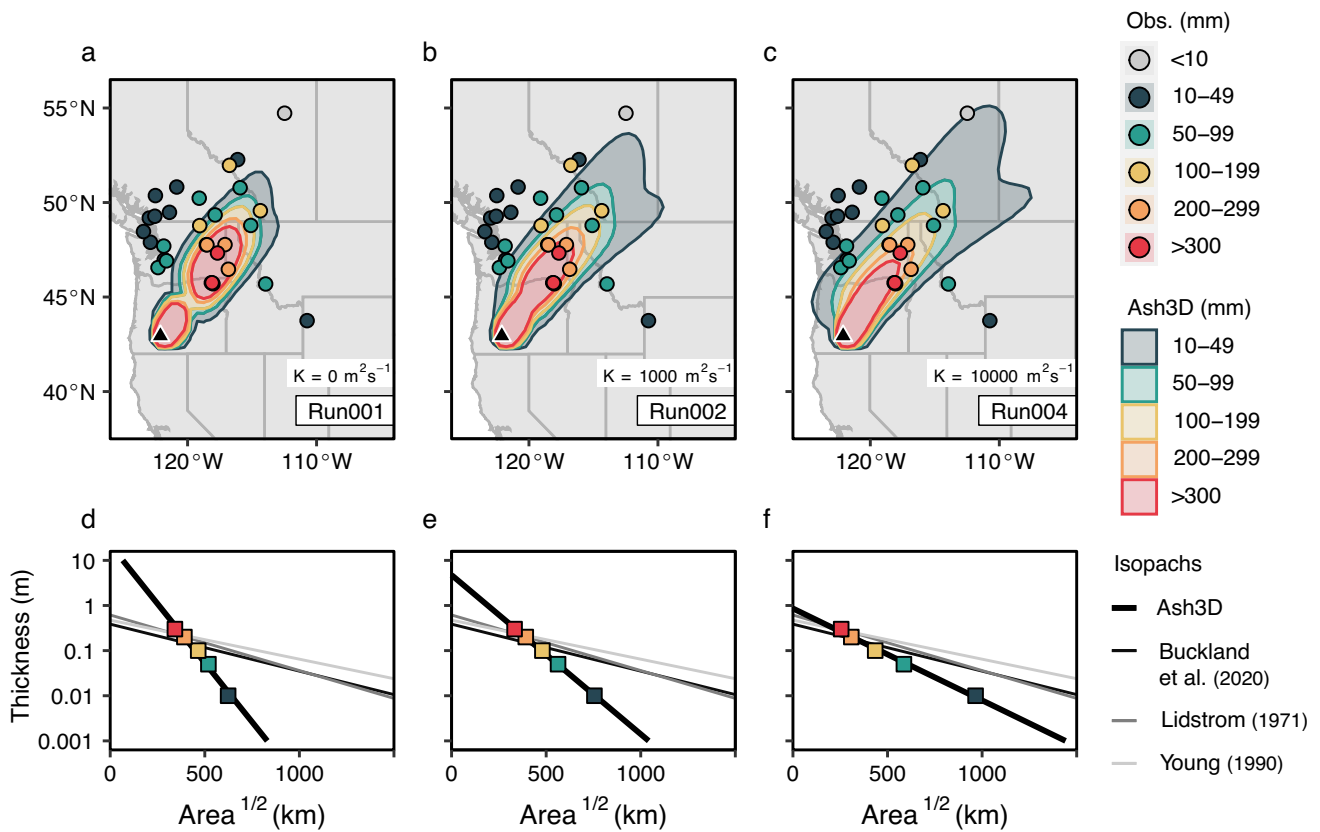


**Fig. 8** Ash3D sensitivity to diffusion constant. Maps of the simulated tephra fall from an eruption of Mount Mazama using a diffusion coefficient of (a) 0, (b) 1000 and (c) 10,000  $\text{m}^2\text{s}^{-1}$ . The coloured points correspond to intervals of ash thickness in mm. (d–f) Square root isopach area versus thickness plots showing data for the 300-,

200-, 100-, 50- and 10-mm isopachs fitted with an exponential function (Pyle 1989; Daggitt et al. 2014). Also plotted are the exponential functions fit to the data for the isopachs reported by Lidstrom (1971) and Young (1990). These plots will be referred to as ‘Pyle plots’ in the subsequent figure captions

from Jenny Lake, Wyoming, USA (site 42 in Fig. 1a), suggest deposition of ~ 1 cm of primary Mazama tephra (Larsen et al. 2016), whereas a maximum 0.2 cm of tephra was estimated by the Ash3D simulations. This mismatch may be caused, in part, by ash dispersion towards the east and southeast during earlier stages of the Mazama eruption (Young 1990). We note, however, that a thickness mismatch at a single distal point does not detract from the overall success of simulating the main dispersal direction of the deposit. More generally, using modern wind data to simulate the prehistoric eruptions requires the assumption that seasonal wind patterns and other atmospheric properties, such as tropopause height and vertical variations in average wind velocity, have not changed since the time of the eruption. These assumptions may be a significant obstacle to using VATDMs to reconstruct prehistoric tephra deposits, particularly pre-Holocene and for regions that have undergone pronounced climate variability.

Simulating umbrella spreading (Fig. 9) and increasing the diffusion coefficient (Fig. 8) in the Ash3D simulations were required to recreate the wide isopachs and significant

off-axis spreading of the Mazama tephra observed in the field (Fig. 1, Buckland et al. 2020). This demonstrates that simply modelling the advection–diffusion of ash following a large magnitude eruption, with no consideration of umbrella cloud spreading, could significantly underestimate the area impacted by ash deposition (Costa et al. 2013; Mastin et al. 2014; Barker et al. 2019; Webster et al. 2020). Currently, most VATDMs used operationally by Volcanic Ash Advisory Centres models ignore umbrella cloud spreading because most eruptions do not produce large umbrella clouds. Yet aircraft encounters within the umbrella area of eruptions at Pinatubo in 1991 (Casadevall et al. 1996) and Kelut in 2014 (Kristiansen et al. 2015), and the significant umbrella cloud produced by the January 2022 eruption at Hunga Tonga-Hunga Ha ‘apai (HTHH; Global Volcanism Program 2022), demonstrate the importance of this process to hazard mitigation.

The Ash3D simulations of the Mazama tephra that use the GSDs based on field data produce the simulations with the smallest divergence between the observed and modelled thickness (Figs. 11 and 12). For example, at site 73 (30 cm

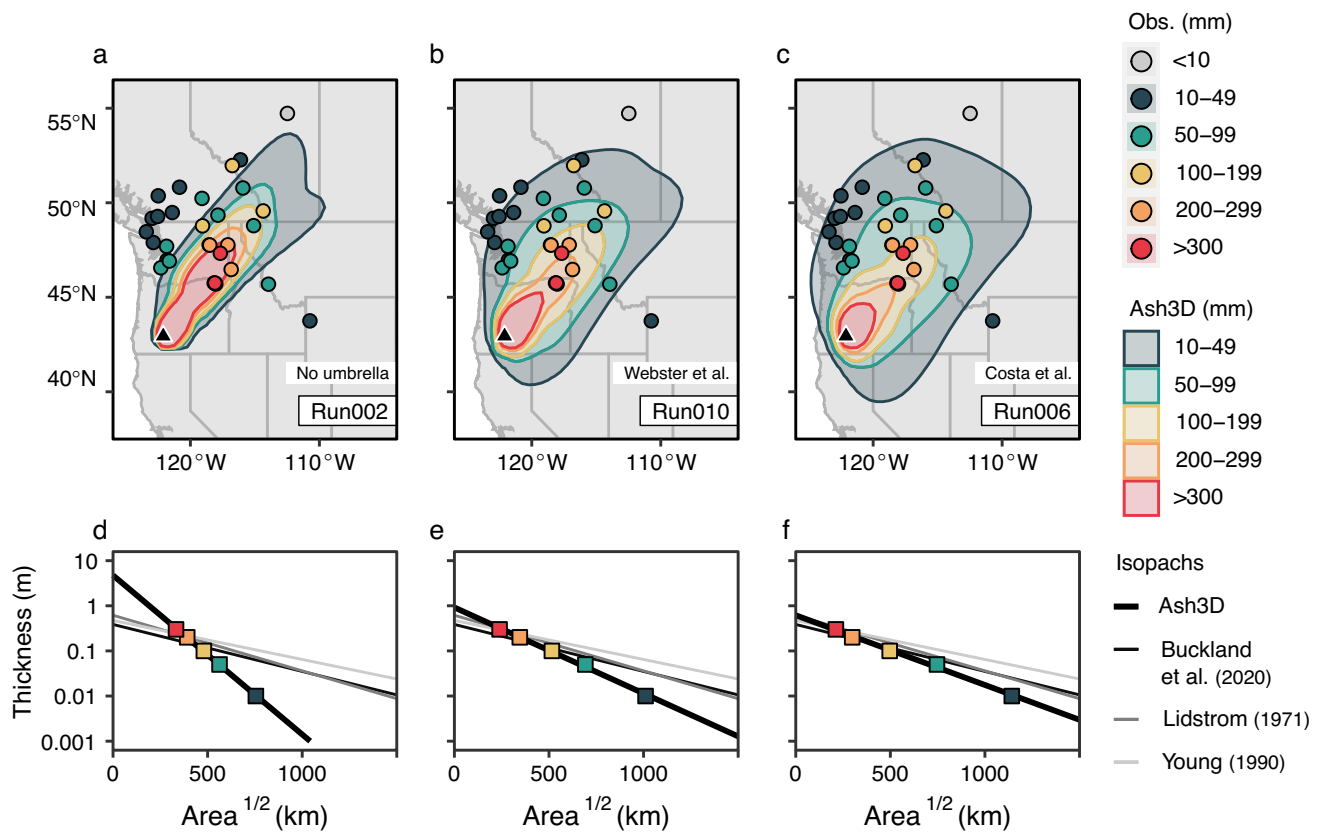


**Fig. 9** Ash3D sensitivity to umbrella spreading rate. Maps of simulated tephra fall from an eruption of Mount Mazama using different umbrella spreading schemes (a) no umbrella spreading, (b) radial spreading using formulation from Webster et al. (2020) and (c) radial

spreading using formulation from Costa et al. (2013). (d–f) Related Pyle plots for panels a–c. The colours and symbology are the same as Fig. 8

measured), only the simulations that use the GSDs based on field data from the Mazama tephra predict > 21 cm of tephra (Fig. 13d, e). This is because generic GSDs over-represent the portion of the total eruption mass that is > 250  $\mu\text{m}$  (Fig. 5), which means more mass is deposited close to source and less mass is transported to the distal region (> 130 km from source). Acquiring GSDs from extensive distal tephra deposits may prove challenging for large magnitude eruptions other than the Mazama tephra, particularly if the distal deposit has been deposited offshore. In this regard, the observation that the GSD of distal tephra remains constant beyond a critical distance from source (Engwell and Eychenne 2016; Cashman and Rust, 2020; Buckland et al. 2021) means that even sparsely distributed data from the distal region can inform GSDs for modelling distal tephra deposits.

Site 73 is a key locality for comparisons against the Ash3D simulations as it records the primary thickness and the GSD has been measured using both laser diffraction (Buckland et al. 2020) and DIA (Buckland et al. 2021). The discrepancy between the simulated and observed GSDs at site 73 (Fig. 13e) indicates that the Ash3D model

is dispersing coarser grains farther than observed in the field. This discrepancy is surprising given that most processes not modelled, such as particle aggregation or gravitational instabilities, tend to accelerate rather than retard ash removal. The over-representation of coarse ash could be caused by poor characterisation of the drag coefficient acting on the ash particles. For example, we assume that the 2D aspect ratio ( $b/l$ ) measured using DIA (Buckland et al. 2021) is equivalent to the 3D shape factor from Wilson and Huang (1979). But, as with size parameters (Buckland et al. 2021), converting from 2 to 3D can poorly characterise the irregularity of the particles and mean that higher drag coefficients and lower terminal velocities are calculated (Saxby et al. 2018). Another explanation for coarse particles reaching farther than observed could be that the umbrella spreading regimes overestimate the absolute velocity and distance over which the umbrella winds influence ash dispersion. For instance, the Costa et al. (2013) spreading regime predicts a higher proportion of particles > 250  $\mu\text{m}$  at site 73 than the Webster et al. (2020) formulation because it models higher radial wind-speeds

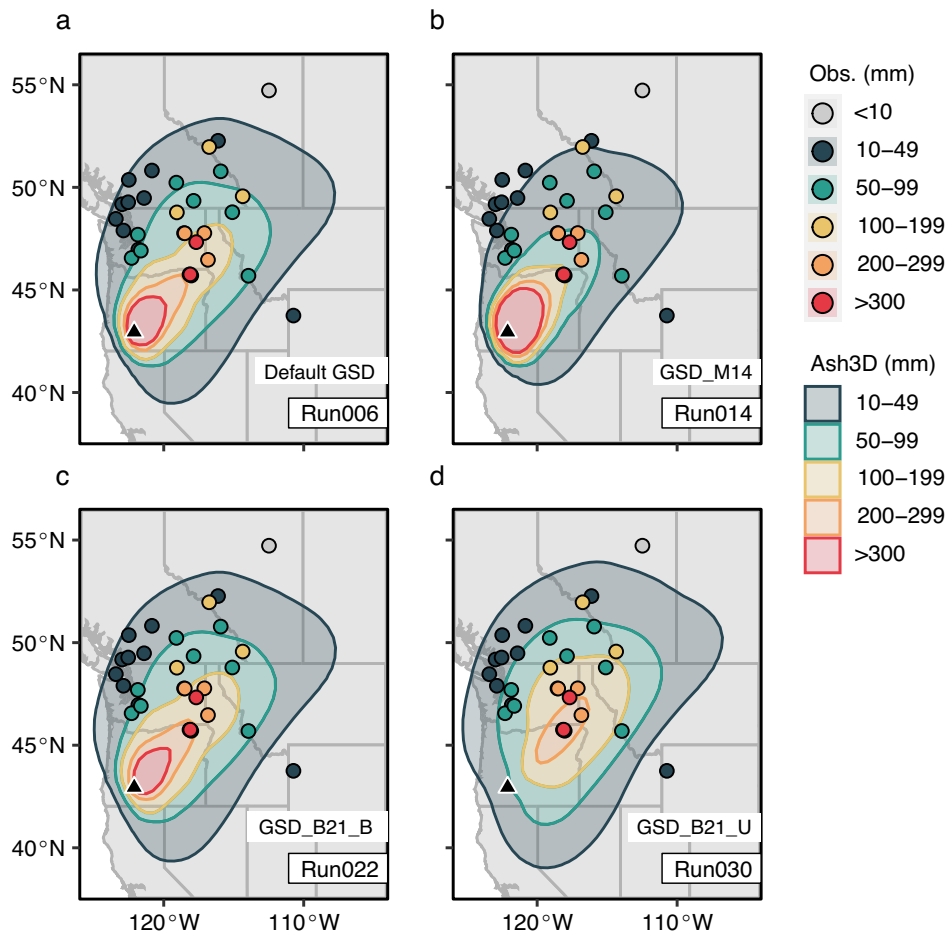


**Fig. 10** Ash3D sensitivity to grain size distribution. Maps of the simulated tephra fall from an eruption of Mount Mazama using the grain size distribution (a) GSD\_M16 (Ash3D default; Fig. 5a; Mastin et al. 2016), (b) GSD\_M14 (Fig. 5b; Mastin et al. 2014), (c) GSD\_B21\_B

(bimodal; Fig. 5c) and (d) GSD\_B21\_U (unimodal; Fig. 5d) TGSDs from field deposits of Mazama tephra (Buckland et al. 2021; Buckland 2022)

close to source (Fig. 3). These findings suggest that further testing of umbrella cloud spreading regimes is required. Future and recent modern eruptions that produce an umbrella cloud could provide an opportunity for such studies if the wind data, umbrella cloud spreading rate and deposit characteristics are well documented both during and immediately after the eruption using field and remote sensing techniques.

### Considering the impact of VATDM simplifications

A significant simplification required to simulate the Mazama tephra deposit using Ash3D is that all ash < 125- $\mu$ m aggregates. This assumption is necessary because if the fine ash is not aggregated, the terminal velocity of the individual particles is so low that it cannot overcome the vertical component of atmospheric velocity (turbulence) and ash < 125  $\mu$ m is

not deposited within the model domain. There is very little evidence, however, of aggregation being the main driver for the sedimentation of the distal Mazama tephra. For example, there are no records of accretionary lapilli across the expansive deposit and little to no fine ash is contained in the fall deposits close to source (< 130 km; Young 1990). This suggests that in addition to aggregation by electrostatic forces (which will not be preserved in the tephra record), other mechanisms resulted in the deposition of the fine-grained distal tephra, such as convective instabilities (Manzella et al. 2015; Scollo et al. 2017; Freret-Lorgeril et al. 2020) and the entrainment of fine material in the wake of coarser particles (Rose et al. 2008; Eychenne et al. 2015).

For the Ash3D simulations, we assumed a single Plinian eruption to avoid uncertainty in the mass attributed to different phases of the eruption (Buckland et al. 2021; Buckland 2022). Further insight could be gained by separately

**Table 2** Significant Ash3D simulations for model sensitivity testing

	Height umbrella cloud ( $H_u$ , km)	Umbrella spreading regime	GSD	Diffusion ( $\text{m}^2\text{s}^{-1}$ )	Deposit density ( $\text{kgm}^{-3}$ )	Figure
Run001	40*	None	GSD_M16	0	1000	8
Run002	40*	None	GSD_M16	1000	1000	8, 9
Run004	40*	None	GSD_M16	10,000	1000	8
Run006	30	Costa et al. (2013)	GSD_M16	1000	1000	9, 10–13
Run010	30	Webster et al. (2020)	GSD_M16	1000	1000	9
Run014	30	Costa et al. (2013)	GSD_M14	1000	1000	10–13
Run022	30	Costa et al. (2013)	GSD_B21_B	1000	1000	10–13
Run030	30	Costa et al. (2013)	GSD_B21_U	1000	1000	10–13

\*With no umbrella spreading this height is the top of the plume ( $H_T$ )

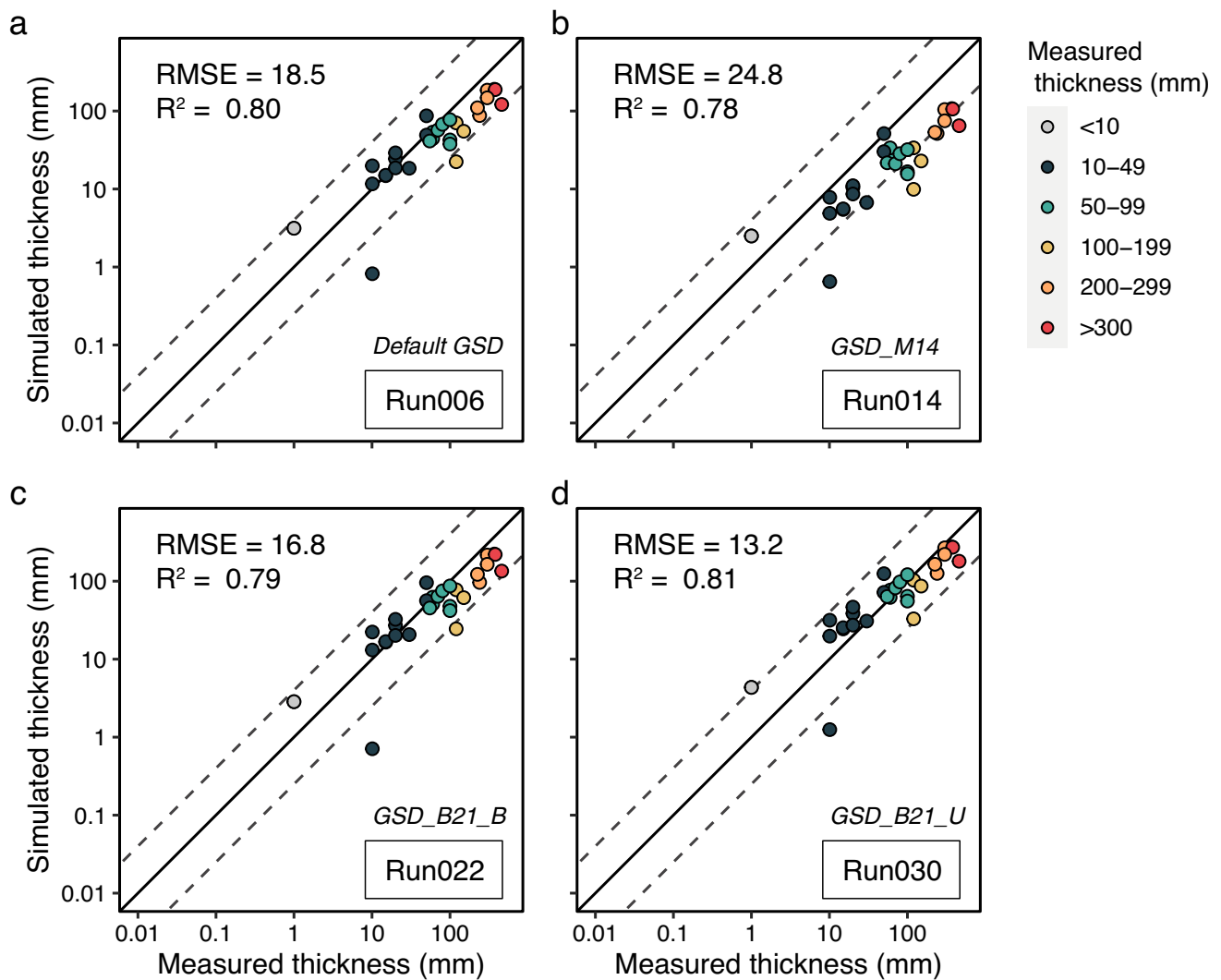


**Fig. 11** Measured versus simulated thicknesses for different grain size distribution (GSD) simulations on log–log scale. Upper and lower dashed lines show values of 4 (over-estimation) and 0.25

(underestimation) times the 1:1 ratio of measured to simulated (solid line). Each panel is labelled with the run number and the  $R^2$  and Root Mean Square Error (RMSE) values

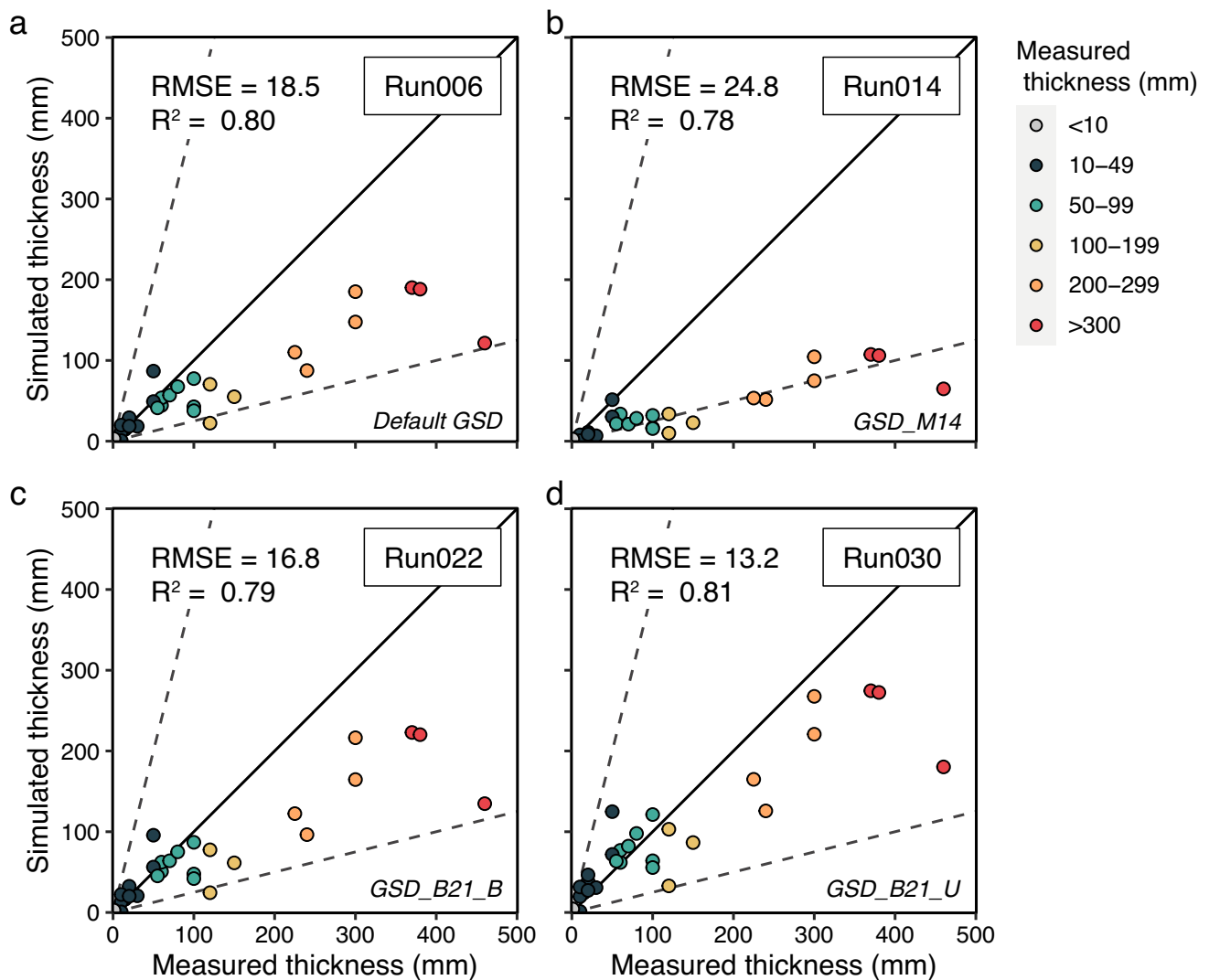


**Fig. 12** Measured versus simulated thicknesses for different grain size distribution (GSD) simulations. Same data as Fig. 11 shown using linear axes

modelling the Plinian and co-PDC eruption phases (Martí et al. 2016). Co-PDC ash tends to be finer than that erupted during Plinian eruptions and can therefore be dispersed over large areas. This could be another explanation for the mismatch between the simulated and observed grain size of distal deposits and provides another reason for using TGSDs derived from distal deposits to approximate distal ash characteristics (Buckland et al. 2021; Buckland 2022). In practice, however, separating and modelling the two eruptive phases present substantial difficulties. For example, there is no chemical variation in the Mazama Plinian and co-PDC products (Young 1990; Buckland et al. 2021; Buckland 2022), which makes the relative deposit proportions from these phases impossible to determine. In addition, source conditions and plume rise processes for Plinian plumes are

considerably different to those from co-PDC plumes, which can loft from the top of entire PDCs resulting in significant mass flow rates (Baines and Sparks 2005; Engwell et al. 2016).

### Conclusions

Using the Ash3D dispersion model, we simulated ash dispersal following the climactic eruption of Mount Mazama using reanalysis meteorological data. We conclude first that using appropriate wind data is crucial to dispersing the Mazama tephra towards the east and northeast of the vent. Notably, we found that modern reanalysis data from northern hemisphere autumn reproduces the main dispersal direction. Though not definitive, this supports a previous assessment of

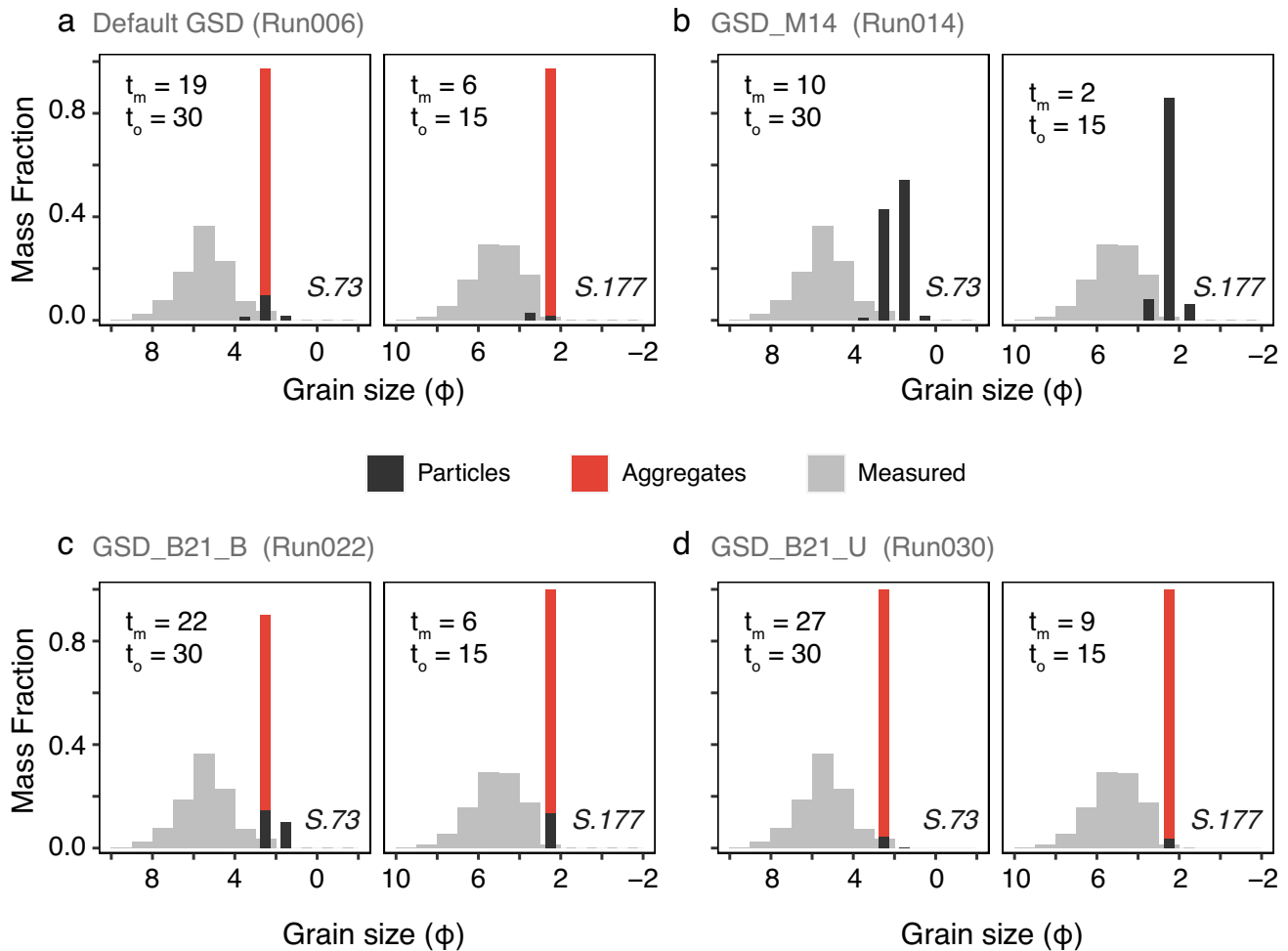


**Fig. 13** Measured grain size distribution (GSD) versus Ash3D GSD for different simulations. Two sites analysed S.73 and S.177.  $t_o$  is the observed thickness and  $t_m$  is the modelled thickness at that site

the eruption seasonality (Mehringer et al. 1997). Secondly, it is necessary to simulate horizontal plume spreading with an umbrella cloud (Costa et al. 2013; Mastin et al. 2014; Webster et al. 2020) to reproduce the significant off-axis spreading of the Mazama tephra deposit. Third, discrepancies between the simulated and observed thicknesses were minimised by using grain size distributions (GSDs) based on the stable grain size distribution of the distal Mazama tephra. Problems remain, however, in the significant simplification that particles  $< 125 \mu\text{m}$  behave like aggregates, for which there is little evidence in the field deposits. Finally, the assumption of a single eruptive phase has likely reduced the accuracy of simulations of the Mazama eruption as an unknown proportion of the distal deposit was probably derived from a co-PDC source.

Future work to improve the accuracy of Volcanic Ash Transport and Dispersion Models (VATDM) for simulating

the ash dispersion from large magnitude eruptions should include additional testing of the equations used to simulate the radial spreading of the umbrella cloud region. Our results conclusively showed that, although it is necessary to include the computation of the radial velocity within the umbrella cloud region of the plume, the question of which formulation of gravitational spreading (Costa et al. 2013; Webster et al. 2020) is the most appropriate remains unclear. Another direction of research required to improve VATDMs is to better understand how fine ash ( $< 125 \mu\text{m}$ ) is deposited. Currently, the simulated aggregation of fines in Ash3D, as in simulations from other VATDM, simplifies the computational complexities of modelling wet and dry aggregation or convective instabilities. However, future advancements in understanding the physics of how fine particles are dispersed and deposited may coincide with increased computational capacity; meaning these physical processes will be

integrated into VATDMs which will improve forecasts of ash transport and deposition for eruptions of any scale.

## Appendix 1. Umbrella spreading regimes

This section contains the formulas used to derive the different spreading regimes used in Ash3D. For the full derivations, see Sparks (1997), Costa et al. (2013) and Webster et al. (2020). The conservation equation of volume for an expanding cylindrical umbrella cloud with time varying radius  $R$  and average cloud thickness  $h$  is given by:

$$\frac{d}{dt}(\pi R^2 h) = q \quad (6)$$

where  $q$  is the volume flow rate into the umbrella cloud. It is assumed that the velocity of the cloud front  $u_R$  scales linearly with the cloud average thickness:

$$u_R = \frac{dR}{dt} = \lambda N h, \quad (7)$$

where  $N$  is the Brunt-Väisälä frequency and  $\lambda$  is an empirical constant reflecting cloud shape.

The spreading of the umbrella cloud is driven by a horizontal pressure gradient between the plume and the ambient atmosphere (Sparks 1997), which is given by:

$$\frac{dP}{dr} = (\rho_c - \rho_a) g \frac{h}{R} \quad (8)$$

where  $\rho_c$  is the density of the umbrella cloud,  $\rho_a$  is the ambient density at the neutral buoyancy level and  $g$  is the gravitational acceleration.

By accounting for the conservation of mass and momentum using Eqs. 6 and 8, Sparks (1997) then derived the following formula for the radius of the umbrella cloud ( $R$ ) fed by a steady column with respect to time ( $t$ ):

$$R = \left( \frac{3\lambda N q}{2\pi} \right)^{\frac{1}{3}} t^{\frac{2}{3}} \quad (9)$$

Finally, by taking the derivative of Eq. 9 with respect to time (Costa et al. 2013; Mastin et al. 2014), the velocity of the cloud's outer margin ( $u_R$ ) with respect to time is given by:

$$u_R = \frac{2}{3} \left( \frac{3\lambda N q}{2\pi} \right)^{\frac{1}{3}} t^{-\frac{1}{3}} \quad (10)$$

**Supplementary Information** The online version contains supplementary material available at <https://doi.org/10.1007/s00445-022-01593-1>.

**Acknowledgements** H.M.B was supported by a NERC GW4+ Doctoral Training Partnership studentship from the Natural Environment Research Council (NERC; NE/L002434/1) with additional support from the British Geological Survey. S.L.E. publishes with permission of the CEO, British Geological Survey, and acknowledges support from British Geological Survey NC-ODA grant NE/R000069/1: Geoscience for Sustainable Futures. K.V.C. acknowledges an AXA Research Fund and a Royal Society Wolfson Merit Award. The manuscript forms one chapter in the doctoral thesis of H.M.B, awarded by the University of Bristol in January 2022 (Buckland 2022). H.M.B produced the estimates of the Eruption Source Parameters and L.M ran the Ash3D simulations. H.M.B has written the main text. L. M, S.L.E and K.V.C have contributed to the writing of the manuscript and discussion of the results. We would like to thank A. Van Eaton who contributed discussion to the early stages of this project and A. Rust has also contributed to the discussion and copy editing of the text. Thanks to B. Jensen and one anonymous reviewer whose constructive comments greatly improved this manuscript. Equally, thanks to J. Crummy and H. Wright who provided internal BGS and USGS reviews that further strengthened the work. And finally, thank you to M. Bursik for their editorial handling of the manuscript. Any use of trade, firm or product names is for descriptive purposes only and does not imply endorsement by the U.S. Government.

**CRedit author contributions** Conceptualization: all authors; methodology: H. Buckland, L. Mastin; data curation: H. Buckland, L. Mastin; formal analysis and investigation: H. Buckland, L. Mastin; writing—original draft preparation: H. Buckland; writing—review and editing: all authors; visualisation: H. Buckland, L. Mastin; funding acquisition: H. Buckland (PhD funding); resources: H. Buckland (field and laboratory investigations), L. Mastin (USGS computing resources); supervision: S. Engwell and K. Cashman (supervising H. Buckland).

**Data availability** The Mazama tephra thickness and grain size, and the input parameters used in each model run, are found in the electronic supplementary material. The wind data use are available online <https://doi.org/10.5066/F7SQ8XKT>. The input, log and output files from the simulations are also available online <https://doi.org/10.5066/P9PVN Y06>.

**Code availability** The code used to process the Ash3D outputs and produce the plots in the main text is available online [https://github.com/HannahBuckland/Ash3D\\_publication](https://github.com/HannahBuckland/Ash3D_publication).

## Declarations

**Competing interests** The authors declare no competing interests.

**Expanding previous work** This manuscript forms one chapter in the doctoral thesis of H. Buckland, awarded by the University of Bristol in January 2022. The work presented here, however, provides more thorough background information about the Mazama eruption and a broader discussion of the results (<https://ethos.bl.uk/OrderDetails.do?uin=uk.bl.ethos.848523>).

**Open Access** This article is licensed under a Creative Commons Attribution 4.0 International License, which permits use, sharing, adaptation, distribution and reproduction in any medium or format, as long as you give appropriate credit to the original author(s) and the source, provide a link to the Creative Commons licence, and indicate if changes were made. The images or other third party material in this article are included in the article's Creative Commons licence, unless indicated otherwise in a credit line to the material. If material is not included in

the article's Creative Commons licence and your intended use is not permitted by statutory regulation or exceeds the permitted use, you will need to obtain permission directly from the copyright holder. To view a copy of this licence, visit <http://creativecommons.org/licenses/by/4.0/>.

## References

- Abella SE (1988) The effect of the Mt. Mazama ashfall on the planktonic diatom community of Lake Washington. *Limnol Oceanogr* 33:1376–1385. <https://doi.org/10.4319/lo.1988.33.6.1376>
- Armienti P, Macedonio G, Pareschi MT (1988) A numerical model for simulation of tephra transport and deposition: applications to May 18, 1980, Mount St. Helens eruption. *J Geophys Res Solid Earth* 93:6463–6476. <https://doi.org/10.1029/JB093iB06p06463>
- Bacon CR (1983) Eruptive history of Mount Mazama and Crater Lake Caldera, Cascade Range, U.S.A. *J Volcanol Geotherm Res* 18:57–115. [https://doi.org/10.1016/0377-0273\(83\)90004-5](https://doi.org/10.1016/0377-0273(83)90004-5)
- Bacon CR, Drittt TH (1988) Compositional evolution of the zoned calkalkaline magma chamber of Mount Mazama, Crater Lake, Oregon. *Contrib Mineral Petrol* 98:224–256. <https://doi.org/10.1007/BF00402114>
- Bacon CR, Lanphere MA (2006) Eruptive history and geochronology of Mount Mazama and the Crater Lake region, Oregon. *Geol Soc Am Bull* 118:1331–1359. <https://doi.org/10.1130/B25906.1>
- Baines P, Sparks R (2005) Dynamics of giant volcanic ash clouds from supervolcanic eruptions. *Geophys Res Lett* 32:L24808. <https://doi.org/10.1029/2005GL024597>
- Barker SJ, Eaton ARV, Mastin LG et al (2019) Modeling ash dispersal from future eruptions of Taupo Supervolcano. *Geochem Geophys Geosyst* 20:3375–3401. <https://doi.org/10.1029/2018GC008152>
- Beckett FM, Witham CS, Leadbetter SJ et al (2020) Atmospheric dispersion modelling at the London VAAC: a review of developments since the 2010 Eyjafjallajökull Volcano Ash Cloud. *Atmosphere* 11:352. <https://doi.org/10.3390/atmos11040352>
- Biass S (2018) Tephra2 Inversion. <https://e5k.github.io/codes/utilities/2018/06/06/inversion/>. Accessed 24 Feb 2020
- Biass S, Bonadonna C (2011) A quantitative uncertainty assessment of eruptive parameters derived from tephra deposits: the example of two large eruptions of Cotopaxi volcano, Ecuador. *Bull Volcanol* 73:73–90. <https://doi.org/10.1007/s00445-010-0404-5>
- Blake DM, Wilson TM, Gomez C (2016) Road marking coverage by volcanic ash: an experimental approach. *Environ Earth Sci* 75:1348. <https://doi.org/10.1007/s12665-016-6154-8>
- Blong RJ, Grasso P, Jenkins SF et al (2017) Estimating building vulnerability to volcanic ash fall for insurance and other purposes. *J Appl Volcanol* 6:2. <https://doi.org/10.1186/s13617-017-0054-9>
- Bonadonna C, Biass S, Costa A (2015) Physical characterization of explosive volcanic eruptions based on tephra deposits: propagation of uncertainties and sensitivity analysis. *J Volcanol Geotherm Res* 296:80–100. <https://doi.org/10.1016/j.jvolgeores.2015.03.009>
- Bonadonna C, Connor CB, Houghton BF et al (2005) Probabilistic modeling of tephra dispersal: hazard assessment of a multiphase rhyolitic eruption at Tarawera, New Zealand. *J Geophys Res Solid Earth* 110:B03203. <https://doi.org/10.1029/2003JB002896>
- Bonadonna C, Folch A, Loughlin S (2012) Puempel H (2012) Future developments in modelling and monitoring of volcanic ash clouds: outcomes from the first IAVCEI-WMO workshop on Ash Dispersal Forecast and Civil Aviation. *Bull Volcanol* 74:1–10. <https://doi.org/10.1007/s00445-011-0508-6>
- Bonadonna C, Genco R, Gouhier M et al (2011) Tephra sedimentation during the 2010 Eyjafjallajökull eruption (Iceland) from deposit, radar, and satellite observations. *J Geophys Res Solid Earth* 116:B12202. <https://doi.org/10.1029/2011JB008462>
- Bonasia R, Capra L, Costa A et al (2011) Tephra fallout hazard assessment for a Plinian eruption scenario at Volcán de Colima (Mexico). *J Volcanol Geotherm Res* 203:12–22. <https://doi.org/10.1016/j.jvolgeores.2011.03.006>
- Brown RJ, Bonadonna C, Durant AJ (2012) A review of volcanic ash aggregation. *Physics and Chemistry of the Earth, Parts a/b/c* 45:65–78. <https://doi.org/10.1016/j.pce.2011.11.001>
- Buckland HM (2022) Anticipating the formation, transport and deposition of ash from the next large volcanic eruption: lessons from the Mazama tephra. PhD Thesis, University of Bristol. <https://doi.org/10.13140/RG.2.2.20634.93126>
- Buckland HM, Cashman KV, Engwell SL, Rust AC (2020) Sources of uncertainty in the Mazama isopachs and the implications for interpreting distal tephra deposits from large magnitude eruptions. *Bull Volcanol* 82:23. <https://doi.org/10.1007/s00445-020-1362-1>
- Buckland HM, Saxby J, Roche M et al (2021) Measuring the size of non-spherical particles and the implications for grain size analysis in volcanology. *J Volcanol Geotherm Res* 415:107257. <https://doi.org/10.1016/j.jvolgeores.2021.107257>
- Bursik MI, Carey SN, Sparks RSJ (1992) A gravity current model for the May 18, 1980 Mount St. Helens plume. *Geophys Res Lett* 19:1663–1666. <https://doi.org/10.1029/92GL01639>
- Cao Z, Bursik M, Yang Q, Patra A (2021) Simulating the transport and dispersal of volcanic ash clouds with initial conditions created by a 3D plume model. *Front. Earth Sci* 9:704797. <https://doi.org/10.3389/feart.2021.704797>
- Carey S, Sparks R (1986) Quantitative models of the fallout and dispersal of tephra from volcanic eruption columns. *Bull Volcanol* 48:109–125. <https://doi.org/10.1007/BF01046546>
- Carey SN (1996) Modeling of tephra fallout from explosive eruptions. In: Scarpa R, Tilling RI (eds) *Monitoring and Mitigation of Volcano Hazards*. Springer, Berlin, pp 429–461. [https://doi.org/10.1007/978-3-642-80087-0\\_13](https://doi.org/10.1007/978-3-642-80087-0_13)
- Casadevall TJ (1994) The 1989–1990 eruption of Redoubt Volcano, Alaska: impacts on aircraft operations. *J Volcanol Geotherm Res* 62:301–316. [https://doi.org/10.1016/0377-0273\(94\)90038-8](https://doi.org/10.1016/0377-0273(94)90038-8)
- Casadevall TJ, Delos Reyes PJ, Schneider DJ (1996) The 1991 Pinatubo eruptions and their effects on aircraft operations. In: Newhall CG, Punongbaya RS (eds) *Fire and Mud: Eruptions and Lahars of Mount Pinatubo*. Philippine Institute of Volcanology and Seismology, Quezon City and University of Washington Press, Seattle, Philippines, p 1115
- Cashman KV, Rust AC (2020) Far-travelled ash in past and future eruptions: combining tephrochronology with volcanic studies. *J Quat Sci* 35:11–22. <https://doi.org/10.1002/jqs.3159>
- Connor CB, Hill BE, Winfrey B et al (2001) Estimation of volcanic hazards from tephra fallout. *Nat Hazards Rev* 2:33–42. [https://doi.org/10.1061/\(ASCE\)1527-6988\(2001\)2:1\(33\)](https://doi.org/10.1061/(ASCE)1527-6988(2001)2:1(33))
- Connor LJ, Connor CB (2006) Inversion is the key to dispersion: understanding eruption dynamics by inverting tephra fallout. In: Mader HM, Connor CB, Coles SG, Connor LJ (eds) *Statistics in volcanology special publications of IAVCEI, 1*. Geological Society, London, pp 231–242
- Constantinescu R, Hopulele-Gligor A, Connor CB et al (2021) The radius of the umbrella cloud helps characterize large explosive volcanic eruptions. *Commun Earth Environ* 2:1–8. <https://doi.org/10.1038/s43247-020-00078-3>
- Constantinescu R, White JT, Connor CB et al (2022) Uncertainty quantification of eruption source parameters estimated from tephra fall deposits. *Geophys Res Lett* 49:e2021GL097425. <https://doi.org/10.1029/2021GL097425>

- Costa A, Dell'Erba F, Di Vito MA et al (2008) Tephra fallout hazard assessment at the Campi Flegrei caldera (Italy). *Bull Volcanol* 71:259. <https://doi.org/10.1007/s00445-008-0220-3>
- Costa A, Folch A, Macedonio G (2013) Density-driven transport in the umbrella region of volcanic clouds: implications for tephra dispersion models. *Geophys Res Lett* 40:1–5. <https://doi.org/10.1002/grl.50942>
- Costa A, Suzuki YJ, Koyaguchi T (2018) Understanding the plume dynamics of explosive super-eruptions. *Nat Commun* 9:654. <https://doi.org/10.1038/s41467-018-02901-0>
- Costa A, Pioli L, Bonadonna C (2017) Corrigendum to “Assessing tephra total grain-size distribution: Insights from field data analysis” [*Earth Planet Sci Lett* 443 (2016) 90–107]. *Earth Planet Sci Lett* 465:205–209. <https://doi.org/10.1016/j.epsl.2017.03.003>
- Costa A, Smith VC, Macedonio G, Matthews NE (2014) The magnitude and impact of the Youngest Toba Tuff super-eruption. *Front Earth Sci* 2. <https://doi.org/10.3389/feart.2014.00016>
- Cressman LS, Cole DL, Davis WA et al (1960) Cultural sequences at the Dalles, Oregon: a contribution to Pacific Northwest Prehistory. *Trans Am Philos Soc* 50:1–108
- Dacre HF, Grant AL, Hogan RJ et al (2011) Evaluating the structure and magnitude of the ash plume during the initial phase of the 2010 Eyjafjallajökull eruption using lidar observations and NAME simulations. *J Geophys Res Atmospheres* 116:D00U03. <https://doi.org/10.1029/2011JD015608>
- Daggitt ML, Mather TA, Pyle DM, Page S (2014) AshCalc—a new tool for the comparison of the exponential, power-law and Weibull models of tephra deposition. *J Appl Volcanol* 3:7. <https://doi.org/10.1186/2191-5040-3-7>
- Druitt TH, Bacon CR (1989) Petrology of the zoned calcalkaline magma chamber of Mount Mazama, Crater Lake, Oregon. *Contrib Mineral Petrol* 101:245–259
- Druitt TH, Bacon CR (1986) Lithic breccia and ignimbrite erupted during the collapse of Crater Lake Caldera, Oregon. *J Volcanol Geotherm Res* 29:1–32. [https://doi.org/10.1016/0377-0273\(86\)90038-7](https://doi.org/10.1016/0377-0273(86)90038-7)
- Durant AJ, Rose WI, Sarna-Wojcicki AM et al (2009) Hydrometeor-enhanced tephra sedimentation: constraints from the 18 May 1980 eruption of Mount St. Helens. *J Geophys Res Solid Earth* 114:B03204. <https://doi.org/10.1029/2008JB005756>
- Engwell SL, de' Michieli Vitturi M, Esposti Ongaro T, Neri A (2016) Insights into the formation and dynamics of coignimbrite plumes from one-dimensional models. *J Geophys Res Solid Earth* 121:4211–4231. <https://doi.org/10.1002/2016JB012793>
- Engwell S, Eychenne J (2016) Contribution of fine ash to the atmosphere from plumes associated with pyroclastic density currents. In: Cashman K, Ricketts H, Rust A, Watson M (eds) *Shona M. Volcanic Ash*, Elsevier, pp 67–85. <https://doi.org/10.1016/B978-0-08-100405-0.00007-0>
- Engwell SL, Sparks RSJ, Aspinall WP (2013) Quantifying uncertainties in the measurement of tephra fall thickness. *J Appl Volcanol* 2:5. <https://doi.org/10.1186/2191-5040-2-5>
- Engwell SL, Sparks RSJ, Carey S (2014) Physical characteristics of tephra layers in the deep sea realm: the Campanian Ignimbrite eruption. *Geol Soc Lond Spec Publ* 398:47–64. <https://doi.org/10.1144/SP398.7>
- Eychenne J, Cashman K, Rust A, Durant A (2015) Impact of the lateral blast on the spatial pattern and grain size characteristics of the 18 May 1980 Mount St. Helens fallout deposit. *J Geophys Res Solid Earth* 120:6018–6038. <https://doi.org/10.1002/2015JB012116>
- Fierstein J, Hildreth W (1992) The plinian eruptions of 1912 at Novarupta, Katmai National Park, Alaska. *Bull Volcanol* 54:646–684. <https://doi.org/10.1007/BF00430778>
- Fierstein J, Nathenson M (1992) Another look at the calculation of fallout tephra volumes. *Bull Volcanol* 54:156–167. <https://doi.org/10.1007/BF00278005>
- Folch A, Cavazzoni C, Costa A, Macedonio G (2008) An automatic procedure to forecast tephra fallout. *J Volcanol Geotherm Res* 177:767–777. <https://doi.org/10.1016/j.jvolgeores.2008.01.046>
- Folch A, Costa A, Basart S (2012) Validation of the FALL3D ash dispersion model using observations of the 2010 Eyjafjallajökull volcanic ash clouds. *Atmos Environ* 48:165–183. <https://doi.org/10.1016/j.atmosenv.2011.06.072>
- Freret-Logeril V, Gilchrist J, Donnadiou F et al (2020) Ash sedimentation by fingering and sediment thermals from wind-affected volcanic plumes. *Earth Planet Sci Lett* 534:116072. <https://doi.org/10.1016/j.epsl.2020.116072>
- Froggatt PC (1982) Review of methods of estimating rhyolitic tephra volumes; applications to the Taupo volcanic zone, New Zealand. *J Volcanol Geotherm Res* 14:301–318. [https://doi.org/10.1016/0377-0273\(82\)90067-1](https://doi.org/10.1016/0377-0273(82)90067-1)
- Global Volcanism Program (2022) Report on Hunga Tonga-Hunga Ha'apai (Tonga). <https://volcano.si.edu/ShowReport.cfm?doi=10.5479/si.GVP.WVAR20220119-243040>. Accessed 8 Feb 2022
- Gouhier M, Eychenne J, Azzaoui N et al (2019) Low efficiency of large volcanic eruptions in transporting very fine ash into the atmosphere. *Sci Rep* 9:1–12. <https://doi.org/10.1038/s41598-019-38595-7>
- Gudmundsson MT, Thordarson T, Höskuldsson Á et al (2012) Ash generation and distribution from the April–May 2010 eruption of Eyjafjallajökull, Iceland. *Sci Rep* 2:572. <https://doi.org/10.1038/srep00572>
- Hadley D, Hufford GL, Simpson JJ (2004) Resuspension of relic volcanic ash and dust from Katmai: still an aviation hazard. *Weather Forecast* 19:829–840. [https://doi.org/10.1175/1520-0434\(2004\)019%3c0829:RORVAA%3e2.0.CO;2](https://doi.org/10.1175/1520-0434(2004)019%3c0829:RORVAA%3e2.0.CO;2)
- Hammer CU, Clausen HB, Dansgaard W (1980) Greenland ice sheet evidence of post-glacial volcanism and its climatic impact. *Nature* 288:230–235. <https://doi.org/10.1038/288230a0>
- Holasek RE, Self S, Woods AW (1996) Satellite observations and interpretation of the 1991 Mount Pinatubo eruption plumes. *J Geophys Res Solid Earth* 101:27635–27655. <https://doi.org/10.1029/96JB01179>
- Hort M (2016) VAAC Operational Dispersion Model Configuration Snapshot (Version 2). [https://www.researchgate.net/publication/324418688\\_VAAC\\_Operational\\_Dispersion\\_Model\\_Configuration\\_Snap\\_Shot\\_2016](https://www.researchgate.net/publication/324418688_VAAC_Operational_Dispersion_Model_Configuration_Snap_Shot_2016)
- Horwell C (2007) Grain-size analysis of volcanic ash for the rapid assessment of respiratory health hazard. *J Environ Monit* 9:1107–1115. <https://doi.org/10.1039/B710583P>
- Horwell CJ, Baxter PJ (2006) The respiratory health hazards of volcanic ash: a review for volcanic risk mitigation. *Bull Volcanol* 69:1–24. <https://doi.org/10.1007/s00445-006-0052-y>
- Houghton BF, Wilson CJN, Fierstein J, Hildreth W (2004) Complex proximal deposition during the Plinian eruptions of 1912 at Novarupta, Alaska. *Bull Volcanol* 66:95–133. <https://doi.org/10.1007/s00445-003-0297-7>
- Jenkins S, Magill C, McAneney J, Blong R (2012) Regional ash fall hazard I: a probabilistic assessment methodology. *Bull Volcanol* 74:1699–1712. <https://doi.org/10.1007/s00445-012-0627-8>
- Jensen BJL, Beaudoin AB, Clynne MA et al (2019) A re-examination of the three most prominent Holocene tephra deposits in western Canada: Bridge River, Mount St. Helens Yn and Mazama. *Quat Int* 500:83–95. <https://doi.org/10.1016/j.quaint.2019.03.017>
- Jensen BJL, Davies LJ, Nolan C et al (2021) A latest Pleistocene and Holocene composite tephrostratigraphic framework for north-eastern North America. *Quatern Sci Rev* 272:107242. <https://doi.org/10.1016/j.quascirev.2021.107242>
- Johnston EN, Phillips JC, Bonadonna C, Watson IM (2012) Reconstructing the tephra dispersal pattern from the Bronze Age eruption of Santorini using an advection–diffusion model. *Bull Volcanol* 74:1485–1507. <https://doi.org/10.1007/s00445-012-0609-x>

- Johnston EN, Sparks RSJ, Phillips JC, Carey S (2014) Revised estimates for the volume of the Late Bronze Age Minoan eruption, Santorini, Greece. *J Geol Soc* 171:583–590. <https://doi.org/10.1144/jgs2013-113>
- Kalnay E, Kanamitsu M, Kistler R et al (1996) The NCEP/NCAR 40-Year Reanalysis Project. *Bull Am Meteor Soc* 77:437–472. [https://doi.org/10.1175/1520-0477\(1996\)077%3c0437:TNYRP%3e2.0.CO;2](https://doi.org/10.1175/1520-0477(1996)077%3c0437:TNYRP%3e2.0.CO;2)
- Kandlbauer J, Sparks RSJ (2014) New estimates of the 1815 Tambora eruption volume. *J Volcanol Geotherm Res* 286:93–100. <https://doi.org/10.1016/j.jvolgeores.2014.08.020>
- Karlstrom L, Wright HM, Bacon CR (2015) The effect of pressurized magma chamber growth on melt migration and pre-caldera vent locations through time at Mount Mazama, Crater Lake, Oregon. *Earth Planet Sci Lett* 412:209–219. <https://doi.org/10.1016/j.epsl.2014.12.001>
- Klawonn M, Houghton BF, Swanson DA et al (2014) From field data to volumes: constraining uncertainties in pyroclastic eruption parameters. *Bull Volcanol* 76:839. <https://doi.org/10.1007/s00445-014-0839-1>
- Klug C, Cashman K, Bacon C (2002) Structure and physical characteristics of pumice from the climactic eruption of Mount Mazama (Crater Lake), Oregon. *Bull Volcanol* 64:486–501. <https://doi.org/10.1007/s00445-002-0230-5>
- Koyaguchi T, Ohno M (2001) Reconstruction of eruption column dynamics on the basis of grain size of tephra fall deposits: 2. Application to the Pinatubo 1991 eruption. *J Geophys Res Solid Earth* 106:6513–6533. <https://doi.org/10.1029/2000JB900427>
- Kristiansen NI, Prata AJ, Stohl A, Carn SA (2015) Stratospheric volcanic ash emissions from the 13 February 2014 Kelut eruption. *Geophys Res Lett* 42:588–596. <https://doi.org/10.1002/2014GL062307>
- Larsen DJ, Finkenbinder MS, Abbott MB, Ofstun AR (2016) Deglaciation and postglacial environmental changes in the Teton Mountain Range recorded at Jenny Lake, Grand Teton National Park, WY. *Quatern Sci Rev* 138:62–75. <https://doi.org/10.1016/j.quascirev.2016.02.024>
- Lechner P, Tupper A, Guffanti M, Loughlin S, Casadevall T (2017) Volcanic ash and aviation—the challenges of real-time, global communication of a natural hazard. In: Fearnly C, Bird DK, Haynes K, McGuire W, Jolly G (eds) *Observing the volcano world: volcano crisis communication*. Springer, Cham, pp 51–64. [https://doi.org/10.1007/11157\\_2016\\_49](https://doi.org/10.1007/11157_2016_49)
- Legros F, Kelfoun K, Martí J (2000) The influence of conduit geometry on the dynamics of caldera-forming eruptions. *Earth and Planetary Science Letters* 179:53–61. [https://doi.org/10.1016/S0012-821X\(00\)00109-6](https://doi.org/10.1016/S0012-821X(00)00109-6)
- Lichti-Federovich S (1970) The pollen stratigraphy of a dated section of Late Pleistocene lake sediment from central Alberta. *Can J Earth Sci* 7:938–945. <https://doi.org/10.1139/e70-089>
- Lidstrom JW (1971) A new model for the formation of Crater Lake Caldera, Oregon. PhD Thesis, Oregon State University. [https://ir.library.oregonstate.edu/concern/graduate\\_thesis\\_or\\_dissertations/bn999920q](https://ir.library.oregonstate.edu/concern/graduate_thesis_or_dissertations/bn999920q)
- Liu EJ, Cashman KV, Beckett FM et al (2014) Ash mists and brown snow: remobilization of volcanic ash from recent Icelandic eruptions. *J Geophys Res Atmospheres* 119:9463–9480. <https://doi.org/10.1002/2014JD021598>
- Long CJ, Whitlock C, Bartlein PJ, Millsaugh SH (1998) A 9000-year fire history from the Oregon Coast Range, based on a high-resolution charcoal study. *Can J for Res* 28:774–787. <https://doi.org/10.1139/x98-051>
- Macedonio G, Pareschi MT, Santacroce R (1988) A numerical simulation of the Plinian Fall Phase of 79 A.D. eruption of Vesuvius. *J Geophys Res Solid Earth* 93:14817–14827. <https://doi.org/10.1029/JB093iB12p14817>
- Madden-Nadeau AL, Cassidy M, Pyle DM et al (2021) The magmatic and eruptive evolution of the 1883 caldera-forming eruption of Krakatau: integrating field- to crystal-scale observations. *J Volcanol Geotherm Res* 411:107176. <https://doi.org/10.1016/j.jvolgeores.2021.107176>
- Magill C, Mannen K, Connor L et al (2015) Simulating a multi-phase tephra fall event: inversion modelling for the 1707 Hoei eruption of Mount Fuji. *Japan Bull Volcanol* 77:81. <https://doi.org/10.1007/s00445-015-0967-2>
- Manzella I, Bonadonna C, Phillips JC, Monnard H (2015) The role of gravitational instabilities in deposition of volcanic ash. *Geology* 43:211–214. <https://doi.org/10.1130/G36252.1>
- Marti A, Folch A, Costa A, Engwell S (2016) Reconstructing the plinian and co-ignimbrite sources of large volcanic eruptions: A novel approach for the Campanian Ignimbrite. *Sci Rep* 6:21220. <https://doi.org/10.1038/srep21220>
- Mastin LG, Eaton ARV, Lowenstern JB (2014) Modeling ash fall distribution from a Yellowstone supereruption. *Geochem Geophys Geosyst* 15:3459–3475. <https://doi.org/10.1002/2014GC005469>
- Mastin L, Randall M, Schwaiger H, Denlinger R (2013) User's guide and reference to Ash3d: a three-dimensional model for Eulerian atmospheric tephra transport and deposition (ver. 2.0, April 2021): U.S. Geological Survey Open-File Report 2013–1122, p 25. <https://doi.org/10.3133/ofr20131122>
- Mastin LG, Van Eaton AR (2020) Comparing simulations of umbrella-cloud growth and ash transport with observations from Pinatubo, Kelud, and Calbuco Volcanoes. *Atmosphere* 11:1038. <https://doi.org/10.3390/atmos11101038>
- Mastin LG, Van Eaton AR, Durant AJ (2016) Adjusting particle-size distributions to account for aggregation in tephra-deposit model forecasts. *Atmos Chem Phys* 16:9399–9420. <https://doi.org/10.5194/acp-16-9399-2016>
- Mastin LG, Van Eaton AR, Schwaiger HF (2020) A probabilistic assessment of tephra-fall hazards at Hanford, Washington, from a future eruption of Mount St. Helens. U.S. Geological Survey Open-File Report 2020–1133. <https://doi.org/10.3133/ofr20201133>
- Matthews NE, Smith VC, Costa A et al (2012) Ultra-distal tephra deposits from super-eruptions: examples from Toba, Indonesia and Taupo Volcanic Zone, New Zealand. *Quat Int* 258:54–79. <https://doi.org/10.1016/j.quaint.2011.07.010>
- Mehring PJ, Arno SF, Petersen KL (1977) Postglacial history of Lost Trail Pass Bog, Bitterroot Mountains, Montana. *Arct Alp Res* 9:345–368
- Nel P, Righarts M (2008) Natural disasters and the risk of violent civil conflict. *Int Stud Quart* 52:159–185
- Newhall C, Self S, Robock A (2018) Anticipating future Volcanic Explosivity Index (VEI) 7 eruptions and their chilling impacts. *Geosphere* 14:572–603. <https://doi.org/10.1130/GES01513.1>
- Oetelaar GA, Beaudoin AB (2016) Evidence of cultural responses to the impact of the Mazama ash fall from deeply stratified archaeological sites in southern Alberta, Canada. *Quatern Int* 394:17–36. <https://doi.org/10.1016/j.quaint.2014.08.015>
- Osores MS, Folch A, Collini E et al (2013) Validation of the FALL3D model for the 2008 Chaitén eruption using field and satellite data. *Andean Geology* 40:262–276. <https://doi.org/10.5027/andgeoV40n2-a05>
- Panbianco JE, Mendez MJ, Buschiazzi DE et al (2017) Dynamics of volcanic ash remobilisation by wind through the Patagonian steppe after the eruption of Cordón Caulle, 2011. *Sci Rep* 7:45529. <https://doi.org/10.1038/srep45529>
- Pedrazzi D, Sunye-Puchol I, Aguirre-Díaz G et al (2019) The Ilopango Tierra Blanca Joven (TBJ) eruption, El Salvador: VOLCANO-stratigraphy and physical characterization of the major

- Holocene event of Central America. *J Volcanol Geotherm Res* 377:81–102. <https://doi.org/10.1016/j.jvolgeores.2019.03.006>
- Perrotta A, Scarpati C (2003) Volume partition between the Plinian and co-ignimbrite air fall deposits of the Campanian Ignimbrite eruption. *Mineral Petrol* 79:67–78. <https://doi.org/10.1007/s00710-003-0002-8>
- Pierson TC, Major JJ (2014) Hydrogeomorphic effects of explosive volcanic eruptions on drainage basins. *Annu Rev Earth Planet Sci* 42:469–507. <https://doi.org/10.1146/annurev-earth-060313-054913>
- Pouget S, Bursik M, Johnson CG et al (2016) Interpretation of umbrella cloud growth and morphology: implications for flow regimes of short-lived and long-lived eruptions. *Bull Volcanol* 78:1. <https://doi.org/10.1007/s00445-015-0993-0>
- Poulidis AP, Phillips JC, Renfrew IA et al (2018) Meteorological controls on local and regional volcanic ash dispersal. *Sci Rep* 8:6873. <https://doi.org/10.1038/s41598-018-24651-1>
- Prata AJ, Tupper A (2009) Aviation hazards from volcanoes: the state of the science. *Nat Hazards* 51:239–244
- Pyle DM (2000) Sizes of volcanic eruptions. In: Sigurdsson H, Houghton B, McNutt S et al (eds) *The Encyclopedia of Volcanoes*. Academic Press, pp 257–264
- Pyle DM (1989) The thickness, volume and grain size of tephra fall deposits. *Bull Volcanol* 51:1–15
- Pyne-O'Donnell SDF, Hughes PDM, Froese DG et al (2012) High-precision ultra-distal Holocene tephrochronology in North America. *Quatern Sci Rev* 52:6–11. <https://doi.org/10.1016/j.quascirev.2012.07.024>
- Rose WI, Durant AJ (2009) Fine ash content of explosive eruptions. *J Volcanol Geotherm Res* 186:32–39. <https://doi.org/10.1016/j.jvolgeores.2009.01.010>
- Rose WI, Self S, Murrow PJ et al (2008) Nature and significance of small volume fall deposits at composite volcanoes: insights from the October 14, 1974 Fuego eruption, Guatemala. *Bull Volcanol* 70(9):1043–1067. <https://doi.org/10.1007/s00445-007-0187-5>
- Rosi M, Vezzoli L, Castelmennano A, Grieco G (1999) Plinian pumice fall deposit of the Campanian Ignimbrite eruption (Phlegraean Fields, Italy). *J Volcanol Geotherm Res* 91:179–198. [https://doi.org/10.1016/S0377-0273\(99\)00035-9](https://doi.org/10.1016/S0377-0273(99)00035-9)
- Rossi E, Bagheri G, Beckett F, Bonadonna C (2021) The fate of volcanic ash: premature or delayed sedimentation? *Nat Commun* 12:1303. <https://doi.org/10.1038/s41467-021-21568-8>
- Rougier J, Sparks RSJ, Cashman KV, Brown SK (2018) The global magnitude–frequency relationship for large explosive volcanic eruptions. *Earth Planet Sci Lett* 482:621–629. <https://doi.org/10.1016/j.epsl.2017.11.015>
- Saxby J, Beckett F, Cashman K et al (2018) The impact of particle shape on fall velocity: implications for volcanic ash dispersion modelling. *J Volcanol Geotherm Res* 362:32–48. <https://doi.org/10.1016/j.jvolgeores.2018.08.006>
- Schwaiger HF, Denlinger RP, Mastin LG (2012) Ash3d: a finite-volume, conservative numerical model for ash transport and tephra deposition. *J Geophys Res Solid Earth* 117:B04204. <https://doi.org/10.1029/2011JB008968>
- Scollo S, Bonadonna C, Manzella I (2017) Settling-driven gravitational instabilities associated with volcanic clouds: new insights from experimental investigations. *Bull Volcanol* 79:39. <https://doi.org/10.1007/s00445-017-1124-x>
- Sheldrake T (2014) Long-term forecasting of eruption hazards: a hierarchical approach to merge analogous eruptive histories. *J Volcanol Geotherm Res* 286:15–23. <https://doi.org/10.1016/j.jvolgeores.2014.08.021>
- Sigurdsson H, Carey S (1989) Plinian and co-ignimbrite tephra fall from the 1815 eruption of Tambora volcano. *Bull Volcanol* 51:243–270. <https://doi.org/10.1007/BF01073515>
- Smith VC, Isaia R, Engwell SL, Paul G A (2016) Tephra dispersal during the Campanian Ignimbrite (Italy) eruption: implications for ultra-distal ash transport during the large caldera-forming eruption. *Bull Volcanol* 78:45. <https://doi.org/10.1007/s00445-016-1037-0>
- Spano NG, Lane CS, Francis SW, Johnson TC (2017) Discovery of Mount Mazama cryptotephra in Lake Superior (North America): implications and potential applications. *Geology* 45:1071–1074. <https://doi.org/10.1130/G39394.1>
- Sparks RSJ, Brazier S, Huang TC, Muerdter D (1983) Sedimentology of the Minoan deep-sea tephra layer in the Aegean and Eastern Mediterranean. *Mar Geol* 54:131–167. [https://doi.org/10.1016/0025-3227\(83\)90011-7](https://doi.org/10.1016/0025-3227(83)90011-7)
- Sparks RSJ, Bursik M, Carey S et al (1997) *Volcanic plumes*. John Wiley & Sons, Inc., p 557
- Stewart C, Johnston DM, Leonard GS et al (2006) Contamination of water supplies by volcanic ashfall: a literature review and simple impact modelling. *J Volcanol Geotherm Res* 158:296–306. <https://doi.org/10.1016/j.jvolgeores.2006.07.002>
- Suzuki YJ, Costa A, Koyaguchi T (2020) Control of Vent Geometry on the Fluid Dynamics of Volcanic Plumes: Insights From Numerical Simulations. *Geophys Res Lett* 47:e2020GL087038. <https://doi.org/10.1029/2020GL087038>
- Stohl A, Prata A, Eckhardt S et al (2011) Determination of time- and height-resolved volcanic ash emissions and their use for quantitative ash dispersion modeling: the 2010 Eyjafjallajökull eruption. *Atmos Chem Phys* 11:4333–4351. <https://doi.org/10.5194/acp-11-4333-2011>
- Suzuki T (1983) A theoretical model for dispersion of tephra. In: Shimozuru D, Yokoyama I (eds) *Arc volcanism, physics and tectonics*. Terra, Tokyo, pp 95–113
- Suzuki YJ, Koyaguchi T (2009) A three-dimensional numerical simulation of spreading umbrella clouds. *J Geophys Res Solid Earth* 114:B03209. <https://doi.org/10.1029/2007JB005369>
- Van Eaton AR, Mastin LG, Herzog M et al (2015) Hail formation triggers rapid ash aggregation in volcanic plumes. *Nat Commun* 6:7860. <https://doi.org/10.1038/ncomms8860>
- Van Eaton AR, Muirhead JD, Wilson CJN, Cimarelli C (2012) Growth of volcanic ash aggregates in the presence of liquid water and ice: an experimental approach. *Bull Volcanol* 74:1963–1984. <https://doi.org/10.1007/s00445-012-0634-9>
- Waitt RB (2015) *In the path of destruction - eyewitness chronicles of Mount St. Helens*. Washington State Univ. Press, Pullman
- Webster HN, Devenish BJ, Mastin LG et al (2020) Operational modelling of umbrella cloud growth in a Lagrangian volcanic ash transport and dispersion model. *Atmosphere* 11:200. <https://doi.org/10.3390/atmos11020200>
- White JT, Connor CB, Connor L, Hasenaka T (2017) Efficient inversion and uncertainty quantification of a tephra fallout model. *J Geophys Res Solid Earth* 122:281–294. <https://doi.org/10.1002/2016JB013682>
- Williams H (1942) *The Geology of Crater Lake National Park, Oregon: with a reconnaissance of the cascade range southward to Mount Shasta*. Carnegie Institution of Washington Publication 540, p 162
- Williams H, Goles G (1968) Volume of the Mazama ash-fall and the origin of Crater Lake Caldera. In: *Andesite conference guidebook*. Oregon Department of Geological and Mineral Industries. 62:37–41
- Wilson L, Huang TC (1979) The influence of shape on the atmospheric settling velocity of volcanic ash particles. *Earth Planet Sci Lett* 44:311–324. [https://doi.org/10.1016/0012-821X\(79\)90179-1](https://doi.org/10.1016/0012-821X(79)90179-1)
- Wilson TM, Cole JW, Stewart C et al (2011) Ash storms: impacts of wind-remobilised volcanic ash on rural communities and agriculture following the 1991 Hudson eruption, southern Patagonia, Chile. *Bull Volcanol* 73:223–239. <https://doi.org/10.1007/s00445-010-0396-1>

- Wilson TM, Stewart C, Sword-Daniels V et al (2012) Volcanic ash impacts on critical infrastructure. *Phys Chem Earth Parts A/B/C* 45:5–23. <https://doi.org/10.1016/j.pce.2011.06.006>
- Woods AW, Kienle J (1994) The dynamics and thermodynamics of volcanic clouds: theory and observations from the April 15 and April 21, 1990 eruptions of redoubt volcano, Alaska. *J Volcanol Geotherm Res* 62:273–299. [https://doi.org/10.1016/0377-0273\(94\)90037-X](https://doi.org/10.1016/0377-0273(94)90037-X)
- Woods AW, Wohletz K (1991) Dimensions and dynamics of co-ignimbrite eruption columns. *Nature* 350:225
- Wright HM, Bacon CR, Vazquez JA, Sisson TW (2012) Sixty thousand years of magmatic volatile history before the caldera-forming eruption of Mount Mazama, Crater Lake, Oregon. *Contrib Mineral Petrol* 164:1027–1052. <https://doi.org/10.1007/s00410-012-0787-8>
- Young SR (1990) Physical volcanology of Holocene airfall deposits from Mt Mazama, Crater Lake, Oregon. PhD Thesis, University of Lancaster. <https://ethos.bl.uk/OrderDetails.do?uin=uk.bl.ethos.315541>
- Zdanowicz C, Zielinski G, Germani M (1999) Mount Mazama eruption: calendrical age verified and atmospheric impact assessed. *Geology* 27:621–624. [https://doi.org/10.1130/0091-7613\(1999\)027%3c0621:MMECAV%3e2.3.CO;2](https://doi.org/10.1130/0091-7613(1999)027%3c0621:MMECAV%3e2.3.CO;2)